

SYSTEM DESIGN CONSIDERATIONS IN NMR IMAGING

**A Thesis Submitted
In Partial Fulfilment of the Requirements
for the Degree of**

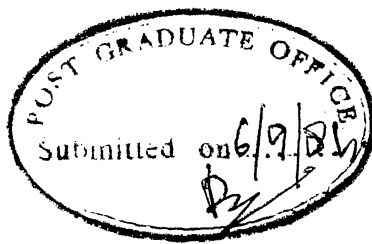
MASTER OF TECHNOLOGY

by

S. KRISHNAN

to the

**DEPARTMENT OF ELECTRICAL ENGINEERING
INDIAN INSTITUTE OF TECHNOLOGY, KANPUR
SEPTEMBER, 1984**



ii

CERTIFICATE

Certified that this work 'SYSTEM DESIGN
CONSIDERATIONS IN NMR IMAGING' by S. Krishnan has been
carried out under my supervision and has not been
submitted elsewhere for a degree.

K.R. Srivathsan

September, 1984.

(K.R. Srivathsan)
Assistant Professor
Department of Electrical Engineering
Indian Institute of Technology
KANPUR

84231

EE-1984-M-KRI-SYS

OCT 1984

A C K N O W L E D G E M E N T S

I am grateful to Dr. K.R. Srivathsan and Dr. P. Raghunathan for suggesting the problem, and for their invaluable guidance and encouragement during the course of work.

My sincere thanks to all my friends, members of the Electrical Engineering Department, and Chemistry Department, for their help.

I would also like to thank Mr. Yogendra, for his neat and careful typing of this thesis.

- S Krishnan

A B S T R A C T

This thesis examines the design considerations of NMR Imaging Systems.

First, a system identification problem for imaging is developed in terms of the Bloch equations and the rotating frame arguments. This shows that

a) The system identification functions (i.e. the spin density distribution $\rho(\vec{r})$ and relaxation times $T_1(\vec{r})$ and $T_2(\vec{r})$) are linearly related to the NMR response.

b) The rf excitation affects the system nonlinearly, and appears as an aperture function in the imaging equation.

The system design is shown as a hierarchy, from the application level, to the system specifications. The case study for a clinical imaging system and a system for study of multiphase bio-samples indicates resolution of 4.5 mm and 1 mm respectively for a frequency resolution of 2 KHz. For the latter the gradient and the rf power dissipation in the coil are shown to be ~ 0.5 G/cm (for a 200 Hz resolution) and 250 W pulsed rms and 10W CW power, respectively. These figures are achievable by using conventional wide-line NMR spectrometers. The imaging modality recommended is the projection reconstruction technique, owing to the ease of signal acquisition.

The coupling circuit design for the rf transceiver, shows stringent requirements in terms of large power, small post-pulse deringing time ($\sim 0.5\mu$ Sec), impedance matching with the power amplifier, and receiver SNR. The use of PIN diodes in series rf switches, is undesirable due to large shot noise (~ 100 pA/ $\sqrt{\text{Hz}}$) introduced. This is one of the reasons for preferring crossed coils in imaging systems, and where space is a premium, other configurations need to be examined.

C O N T E N T S

	Page
Chapter 1 INTRODUCTION	1
1.1 NMR Imaging	1
1.2 Purpose of Work	4
1.3 Organisation of the Thesis	5
Chapter 2 REVIEW OF NMR IMAGING	7
2.1 Historical Background	7
2.2 Theory of NMR	8
1. Quantum Mechanical Interpretation	8
2. Classical Interpretation	11
2.3 Mathematical Model of NMR : The Bloch Equations	15
2.4 Principles of NMR Imaging	17
2.5 A Basic NMR Experiment	20
1. CW NMR	21
2. Pulsed NMR	21
2.6 Spin Echo	23
2.7 Imaging Modalities	26
1. Reconstructive Imaging	27
2. Non-reconstructive Imaging	27
3. Recovery Sequence : T_1 Sensitive Imaging	35
4. Spin Echo Imaging	36
5. Doppler Imaging	36
2.8 Excitations in Imaging	37
1. rf Pulses	37
2. Field Gradients	38

Chapter 3	MATHEMATICAL MODEL OF THE NMR IMAGING SYSTEM	39
3.1	Requirements of the Mathematical Model : NMR as a System Identification Problem	39
3.2	Bloch Equations	41
3.3	The Basic NMR Imaging Equation	44
3.4	A Solution of the Bloch Equations	51
3.5	System Equations for Different Elementary Excitations	55
3.6	FID and NMR Receiver	58
Chapter 4	SYSTEM DESIGN CONSIDERATIONS	68
4.1	System Schematic	68
	1. Main Field Coil System	68
	2. Gradient Coil System	69
	3. rf Coil	72
4.2	General Design Considerations	73
4.3	System Specifications	75
	1. Signal-to-Noise Ratio	77
	2. Magnetic Field H_0	78
	3. Field Gradient and Resolution	80
	4. Signal Level and Transmitted Power	82
	5. Signal Acquisition and Sampling	83
4.4	An Imaging System for Multiphase Bio-samples	85
Chapter 5	A PULSED rf TRANCEIVER	98
5.1	Tranceiver Requirements	98
5.2	rf Coupling Circuit	100

Page

Chapter 6	SUMMARY	110
6.1	Discussion	110
6.2	Suggestions for Future Works	114
	REFERENCES	116
	APPENDIX A	121
	APPENDIX B	125

LIST OF FIGURES

	Page
2.2a Energy Level Splitting Due to H_0 and rf irradiation	10
2.2b Classical Picture of NMR (Laboratory Frame)	10
2.2c Classical Picture of NMR (Rotating Frame)	12
2.3a Principle of NMR Imaging	12
2.3b T_1 and T_2 Dependence	19
2.4 Spin Echo	25
2.5 'Imaging' on the Phase Plane	29
2.6 Imaging Modalities	30 - 31
3.1 Systems Approach	40
3.2 Rotating Frame at Point x	47
3.3 NMR Imaging System	47
3.4 Selective Excitations	62
3.5 Imaging Receiver Schematic	62
3.6 The Received Signal and Noise Spectrum	63
3.7 System Identification Problem	63
4.1 Block Schematic of NMR Imaging System	70
4.2 Some Coil Geometries	71
4.3 A System Design Relationship	76
5.1 A Series Resonance Coupling Circuit	106
5.2 Resonant Circuit with Power Matching	106
5.3 Coupling Circuit Using $\lambda/4$ Section and PIN Diode Switch	107
5.4 Typical Excitation Sequence	107

LIST OF TABLES

		Page
2.1	Reconstructive Imaging	32
2.2	Non-reconstructive Imaging	33-34
4.1	Image Quality and System Parameters	88
4.2	First Order Design Equations	89-92
4.3	Case Study	93-96
4.4	Hardware and System Specification	97
5.1	System Specification	105
5.2	Circuit Values for A, B and C	108-109

LIST OF KEYWORDS AND SYMBOLS

1. NMR Imaging
2. Zeugmatography
3. Tomography
4. Selective Pulse
5. Aperture Function
6. Gyromagnetic Ratio
7. Spin Echo
8. Saturation and Inversion Recovery
9. Relaxation Time
10. Signal to Noise Ratio
11. Resolution
12. Contrast

$\rho(x,y,z)$	Spin Density Distribution (per unit volume)
$T_1(\vec{r})$	Spin-lattice Relaxation Time (T)
$T_2(\vec{r})$	Spin-spin Relaxation Time (T)
v	Velocity in the Sample (LT^{-1})
h	Plank's Constant (6.6×10^{-34} Joules-Sec.)
I	Spin Quantum Number ($=1/2$ for Proton)
M_p	Rest Mass of the Proton (1.67×10^{-27} Kg)
γ	Gyromagnetic Ratio ($2\pi \times 42.576$ Mrad/sec/Tesla for the Proton)
k	Boltzmann's Constant (1.38×10^{-23} J/ $^{\circ}$ K)
M_0	Equilibrium Magnetization ($L^{-1} T^{-1} Q: A-m^{-1}$ $3.25 \times 10^{-3} H_0$ A-m $^{-1}$, for the Protons in water at 310 $^{\circ}$ K)
H_0	Main Magnetic Field
$B_1(t)$	rf Magnetic Field
ΔH	Residual Field in the Rotating Frame
$\vec{G}(\vec{r})$	Magnetic Field Gradient (in Gauss/cm)
ω_0	Larmour Precession Frequency (in Radians/Sec.)

CHAPTER 1

INTRODUCTION

1.1 NMR IMAGING

Nuclear Magnetic Resonance has gained importance as an imaging tool, in chemistry and Medicine after Lauterbur's work in 1973 [1]. He indicated that in the presence of steady magnetic field superimposed by a field gradient, and an orthogonal radio frequency magnetic field, it is possible to extract the information about the spatial, nuclear spin density distribution of the sample under study. The method is termed *Zeugmatography* to denote extraction of density information from field interactions (Zeugma means 'that which joins together' in Greek). The clinical applicability of NMR was shown by Damadian in 1971 [2]. It is seen that certain features of NMR make it attractive to clinical imaging, as compared to other modalities such as Radiography, Computed-Axial-Tomography (X-ray CT), Ultrasound, and Positron Emission Tomography (PET). A. Moss [3] compares these modalities in the light of medical applications.

Briefly NMR Imaging, is an analytical technique, quite similar to NMR spectroscopy. It is able to extract spin density information as a function of spatial location, for different nucleides such as ^1H (proton) and the isotopes ^7Li , ^{13}C , ^{31}P and ^{27}I . In the clinical context it is usually the proton, due to its inherently large SNR in NMR experiments.

In addition there are other observable parameters, describing the state of the system being imaged. They are T_1 , the spin lattice relaxation time, T_2 the spin-spin relaxation time and v the movement in the sample, all functions of spatial location. Through appropriate emphasis on these parameters, different aspects of the system such as contrast may be studied (Macovski [4]). Unlike other imaging methods, spatial resolution in NMR is not primarily dependent on the wavelength of the excitation. The magnitude of the magnetic field gradient, referred hitherto, determines the resolution.

The pros and cons in NMR imaging viz-a-viz, other imaging techniques is listed below. The basic requirements for any imaging method in the clinical context are given by, Ter-Pogossian [5]. The principle of NMR Imaging is found in Cho et al., [6] and Kaufman and Crooks [7], while that for X-ray CT, the technique mainly compared with, is given in Scudder [8].

ADVANTAGES :

1. NMR is non invasive and non hazardous (no detrimental effects of rf fields in the range of 1-15 MHz, the frequency of operation, have been observed).
2. The response is chemical specific, enabling the imaging of distribution of various chemical states of the nucleides.
3. It affects four parameters of measurements,* allowing for better selectivity of the characteristics to be measured.

* vide-supra

4. The dependence of doppler allows selective imaging of sample movements, as in flow measurements. This avoids motion artifacts found in X-ray CT.
5. The imaging modalities are numerous, within the main framework of NMR. This introduces flexibility in different applications.
6. The number of moving parts in the NMR hardware are fewer compared to the high precision linear and rotary motions required in X-ray CT and PET.

DISADVANTAGES :

1. The sensitivity of NMR is ~~inherently~~ lower compared with other imaging schemes.
2. The stringent requirements in maintaining high magnetic fields (H_0 : 3-4 KG) accurate to 1 in 10^5 spatially and temporally. Large magnets for medical applications are made with super conductors, which determine the economics of the imaging system.
3. In many applications NMR is bulky and cumbersome (due to the magnet and power supplies) compared to techniques like Ultrasound Imaging, which is portable.
4. Patients with aids such as the Cardiac pacemaker cannot be imaged due to the large magnetic fields used.

It is predicted (Kaufmann and Crooks [9]), that while Ultrasound and Digital Radiography would continue to occupy an important place in diagnostic medicine, NMR would vie with X-ray CT. Though X-ray CT, has been developed and perfected over a considerable length of time, the commercial viability of NMR Imaging with Protons, is imminent in the foreseeable future. In areas such as in-vivo metabolic studies with ^{31}P and ^{13}C , NMR potentially holds the forte. This area of research however involves engineering problems (such as SNR of the experiment), which needs to be solved.

1.2 Purpose of Work

The object of this thesis is to present a review of different NMR Imaging modalities proposed in literature with a view of evolving a system design.

Attention is focussed on mathematical modelling of NMR imaging. It is compared with the usual linear time invariant models encountered in electronic systems. The problem is seen in the light of system identification approach in the presence of noise. The relevance of this approach to areas such as ^{31}P and ^{13}C imaging is indicated.

An actual system design for a small imaging instrument operating at 3.5 KG (15 MHz) has been carried out. The design considerations involve translation of the application require-

ments (in this case the study of multiphase bio-specimen), to system parameters. Design of the rf transceiver subsystem for this instrument is discussed in detail.

1.3 ORGANIZATION OF THE THESIS

This thesis considers two aspects of NMR imaging, namely the mathematical model, and the system design.

Chapter 2, gives the principles of (NMR and imaging). The various ingredients in an NMR experiment are considered and a brief review of different imaging modalities used, is given.

Chapter 3, develops Bloch's phenomenological equations of NMR as the mathematical model. The rotating frame argument is employed to derive the basic imaging equation and observations regarding the non-linearity of the model, is made. The mathematical formulation for basic excitations, and for different modalities, are listed. Finally the processing of the NMR response, is followed to state the system identification problem.

Chapter 4, considers, the design considerations for the various blocks in the Imaging system. General design requirements are given, followed by the parameter specifications for the detection system, consisting of the rf transceiver

and the signal ^eacquisition system. A case study is presented to quantify different system requirements. The feasibility of a small imaging system for use in study of multiphase bio-samples is considered.

Chapter 5, discusses the rf transceiver system, with emphasis on the coupling circuit design and Chapter 6, highlights the problems considered, alongwith some suggestions for future work.

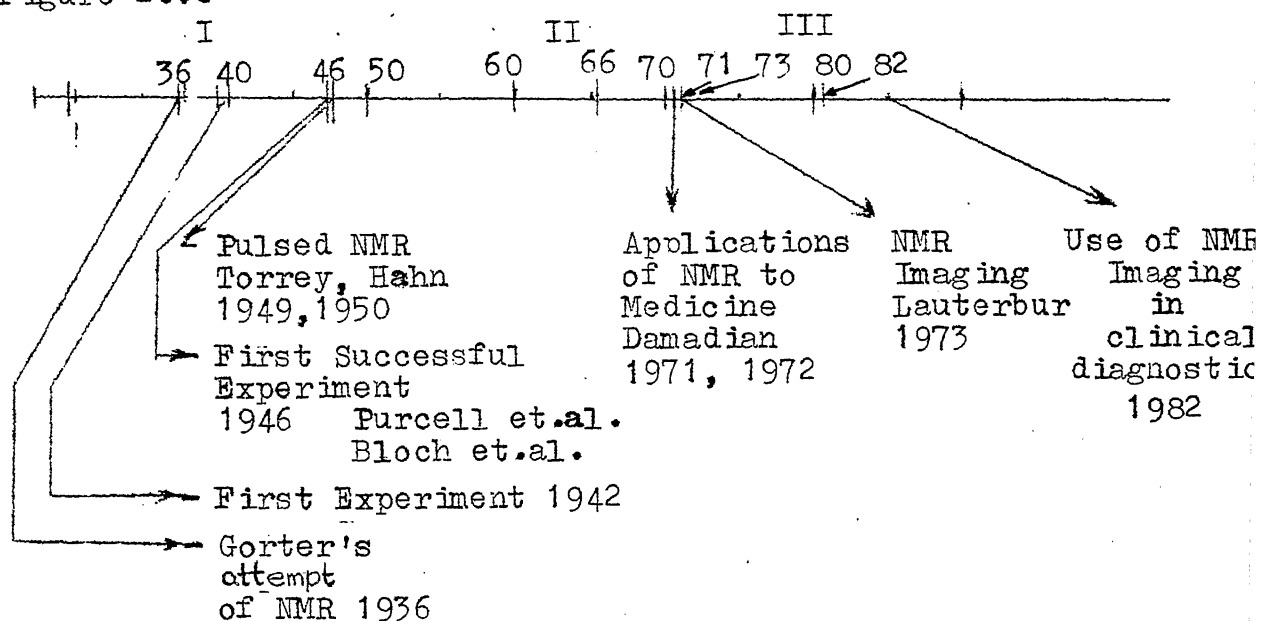
Appendix A presents some details of derivations encountered in Chapter 3 of the thesis.

CHAPTER 2

REVIEW OF NMR IMAGING

2.1 HISTORICAL BACKGROUND

The Nuclear Magnetic Resonance phenomenon in bulk matter was pointed out as early as in 1936 by Gorter. However the first successful NMR experiment was carried out independently by Purcell, Torrey and Pound and by Bloch, Hansen and Packard in 1946. Subsequently the importance of NMR as an analytical tool was realized, and concerted work was underway by 1950's to develop viable instrumentation. A comprehensive description of early NMR spectrometers is found in Andrew [10]. Chronological development in NMR from 1936 till present is given in Figure 2.1.



I : CW NMR, Quantum and Classical Theories of NMR
II: Pulsed NMR and Instrumentation
III: NMR Imaging and Applications to Clinical Diagnostics

Figure 2.1 A Chronology of NMR

The first phase of development was on the phenomenon itself, wherein the techniques used involved CW excitations. The second phase saw the development of pulsed techniques and instrumentation. Many of the standard pulsed spectrometers were first manufactured during this period. The third phase is the application of this technique to imaging and its consequent use in medicine.

2.2 THEORY OF NMR

The NMR phenomenon arises from the splitting in the energy levels of an atom due to the interaction of the nuclear spin with an external magnetic field. Heuristically this interaction may be attributed to the magnetic moment arising in the nuclei having an intrinsic angular momentum. This phenomenon essentially occurs in the quantum domain, and must be rigorously treated as such. However it is useful to adopt the classical arguments to model the phenomenon, especially from the point of view of instrumentation. For the sake of completeness, the quantum mechanical and the classical pictures are presented below [10].

1. QUANTUM MECHANICAL INTERPRETATION

This picture evolves from the concept of the spin angular momentum and the spin quantum number I . The magnitude of the

angular momentum vector of the spinning nucleus is given as $[I(I+1)]^{1/2} \hbar$ where $\hbar \triangleq h/2\pi$, h being the Plank's constant. Though this vector may assume infinite number of directions in space, the measurable component (in the direction of an externally applied magnetic field) is quantized, as $m \hbar$ where m assumes $(2I+1)$ values, from I to $-I$. The corresponding components of the magnetic moment $\mu (= e \hbar / 2M_p c)$ of the nucleus, are given by $m\mu/I$. These components, along with a magnetic field H_0 , give $(2I+1)$ energy levels of magnitude $-m\mu H_0/I$, about the main level. This is the energy level splitting, referred hitherto.

The separation between successive energy levels

$$\Delta E \text{ is, } \Delta E = \frac{\mu H_0}{I}$$

A radiation of frequency ν_0 with energy given by

$$h\nu_0 = \frac{\mu H_0}{I},$$

would lead to an energy level transition marked by a net absorption of energy from the radiation. In the case of protons, which is of interest in this thesis $I = 1/2$ and $h\nu_0 = 2\mu H_0$. The splitting of the energy levels and the emission-absorption feature are illustrated in Figure 2.2a.

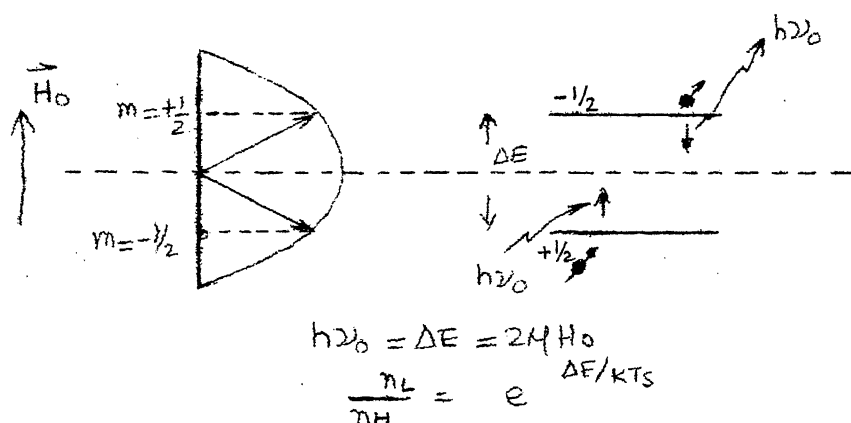


FIGURE 2-2a ENERGY LEVEL SPLITTING DUE TO H_0 AND RF IRRADIATION (QUANTUM PICTURE OF NMR)

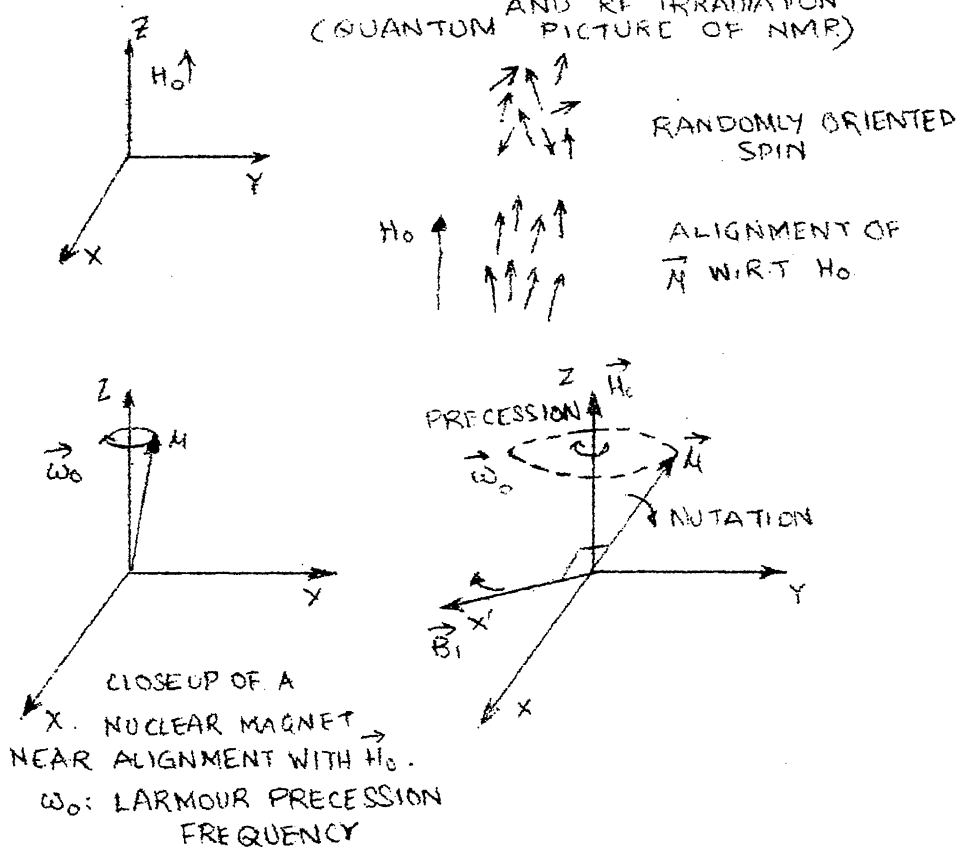


FIGURE 2-2b CLASSICAL PICTURE OF NMR (LABORATORY FRAME)

The discussion thus far has been addressed to the interaction of a single nucleus, with a steady external magnetic field H_0 . On a bulk scale the phenomenon is statistical and follows the Boltzmann distribution for the population among energy levels.

Using the concept of the spin temperature, and the lattice temperature ('lattice' refers to the environment, in which the nuclear spins are embedded), Time constants, T_1 : Spin-Lattice relaxation time and T_2 : Spin-Spin relaxation time and the saturation factor Z , are derived. For details the reader is referred to Andrew [10]. The parameters T_1 and T_2 would be touched upon again in the next section while discussing the classical theory and a mathematical model of NMR.

2. CLASSICAL INTERPRETATION

Notwithstanding the rigour of the quantum mechanical treatment, the classical picture gives useful insight into the phenomenon. As such this approach is employed in the rest of the thesis. A comprehensive treatment is given in Andrew [10].

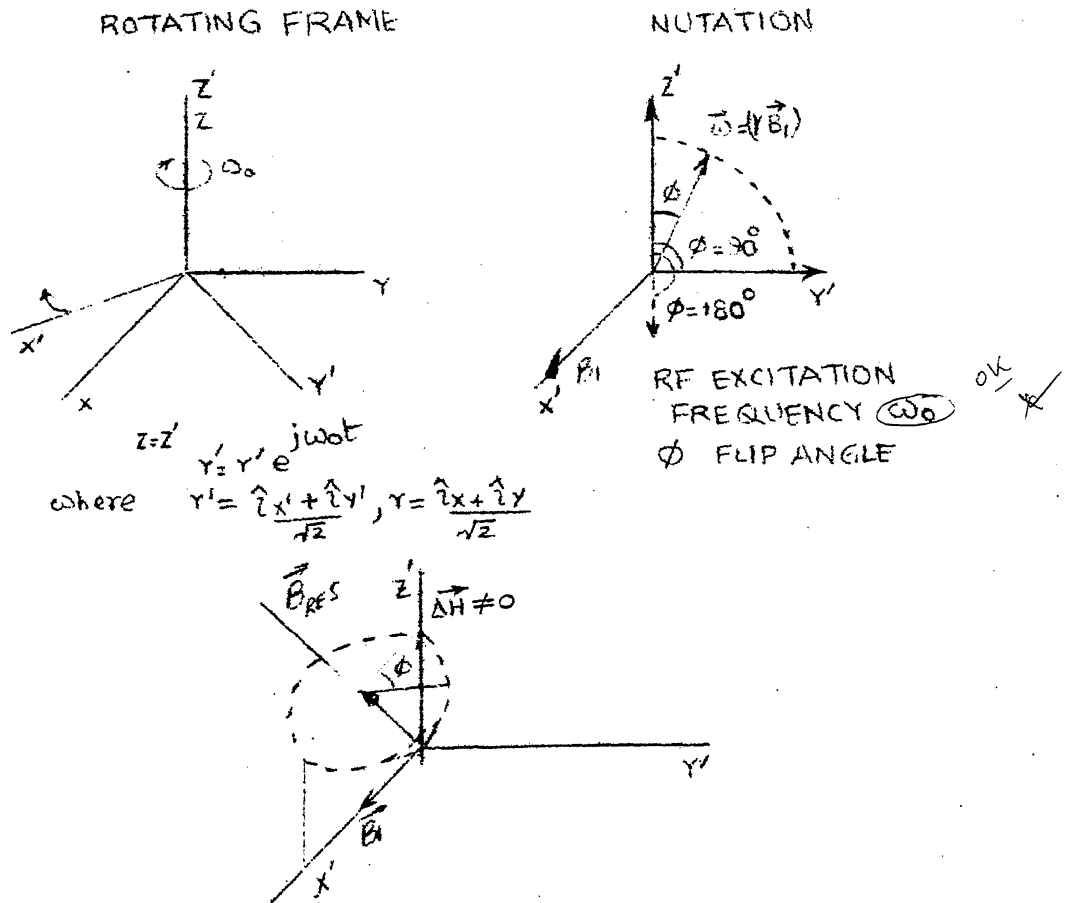


FIGURE 2.2c CLASSICAL PICTURE OF NMR (ROTATING FRAME)

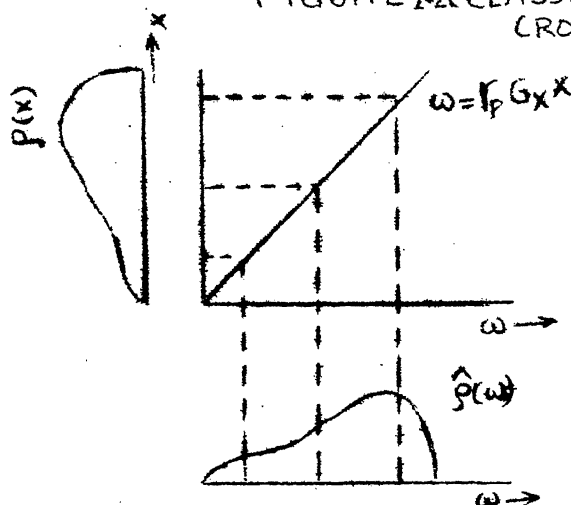


FIGURE 2.3a PRINCIPLE OF NMR IMAGING

In brief, the phenomenon may be visualised as follows (Figures 2.2 b, c):

- In the absence of a magnetic field the elemental magnetic moments (associated with the spin of the nuclei) are randomly oriented in space, the randomness being governed by the temperature of the system.
- On the application of a magnetic field H_0 along the Z' axis, the spins tend to align along the direction of the field, the tendency being opposed by random fluctuations imposed by thermal agitation.
- The nuclear magnetic moment $\vec{\mu}$ experiences a torque proportional to $\vec{\mu} \times \vec{H}_0$, and starts precessing about \vec{H}_0 (or Z axis) at the angular rate $\vec{\omega}_0 = -\gamma \vec{H}_0$, very similar to a rotating top or a gyroscope. The constant γ , termed the gyromagnetic ratio varies with the kind of nucleus participating in the process and is numerically equal to $\mu/I\hbar$, the quantum mechanical counterpart. For the proton $\gamma/2\pi = 42.576$ MHz/Tesla or 4.2576 KHz/Gauss.
- Introduction of a circularly polarized radio-frequency magnetic field \vec{B}_1 (at frequency $\omega = \gamma H_0$), in a plane orthogonal to the Z -axis, tends to rotate the magnetic moment $\vec{\mu}$ about its instantaneous axis. The rotation is termed Nutation in Gyroscopy parlance. This is better

visualized and handled mathematically by adopting a rotating frame of reference. This frame, termed $X'Y'Z'$, rotates about the Z axis at frequency ω_0 in the same sense as the precession of the nuclear magnet, and is implicitly assumed in the rest of the thesis.

Mathematically the precession frequency ω_0 , also called the Larmour frequency is expressed as

$$\vec{\omega}_0^> = -\gamma \vec{H}_0^> \quad \text{in the laboratory frame of reference XYZ.}$$

In the presence of an rf field of frequency ω_0 ,

$$\begin{aligned} \vec{\omega}_{\text{res}}^> &= -\gamma \vec{H}_{\text{res}}^> \\ &= -\gamma (\vec{H}_0^> + \vec{B}_1^>(t)) \text{ in XYZ frame.} \end{aligned}$$

where $\vec{H}_{\text{res}}^>$ denotes the resultant magnetic field.

In the rotating frame

$$\left| \vec{\omega}_{\text{res}}^> \right|_r = \gamma \left| \vec{B}_1^> \right|_{\text{max}}$$

as the effect of $\vec{H}_0^>$ is subsumed in the rotating frame.

$(\vec{\omega}_{\text{res}}^>)_r$ is the Nutation frequency, and is an important variable in NMR.

If the rf-field is applied uniformly for a duration T_p , the angle ϕ by which $\vec{\mu}^>$ nutates is given by

$$\phi = (\gamma \left| \vec{B}_1^>(t) \right| T_p).$$

θ is termed the flip angle. It will be seen that the observation plane in NMR is the XY/X'Y' plane, and consequently to obtain maximum response, θ must be $\pi/2$.

Another flip angle of importance in pulsed NMR studies (where rf-excitation is pulsed) is $\theta = \pi$. These pulses are also called the 90° and 180° pulses for obvious reasons.

Though the picture presented is for a single nucleus, the results may be extended to bulk matter by studying the statistical behaviour. This is incorporated in Bloch's Phenomenological equation discussed below.

2.3 MATHEMATICAL MODEL OF NMR : THE BLOCH EQUATIONS

The model is developed based on the differential equation of motion,

$$\frac{d\vec{\mu}}{dt} = \gamma \vec{\mu} \times \vec{H}$$

Assuming a statistical description on a bulk scale, the equation may be rewritten as

$$\frac{d\vec{M}}{dt} = \gamma \vec{M} \times \vec{H},$$

Where \vec{M} is the net magnetization, instead of $\vec{\mu}$. This denotes the net magnetic moment per unit volume.

At equilibrium

$$|\vec{M}| = M_0 = N \gamma^2 h^2 \frac{H_0}{3 K T_s} I(I+1),$$

which is related to the static susceptibility χ ,

Here N is the number of spins per unit volume,
 γ the gyromagnetic ratio,
 H_0 is the steady magnetic field ,
 I the spin Quantum number ($=\frac{1}{2}$ for protons),
 T_s is the sample temperature.

The numerical value of M_0 is $3.25 \times 10^{-3} \text{ A m}^{-1}/\text{Tesla}$, for protons in water at 310°K .

This is thus a LUMPED MODEL.

Addition of factors describing the spin-lattice and the spin-spin relaxation effects lead to a complete set of phenomenological equations called the Bloch equations. The assumptions made in involving the factors T_1 and T_2 are that, (i) the effects are exponential and may be obtained by a linear superposition. and (ii) T_1 affects the Z-component of the dynamical equations while T_2 affects the X and Y components. The rationale for these assumptions is based on observations, and is that (i) The exponential behaviour is consistent with a simple quantum statistical description. (ii) T_1 is related to restoration of equilibrium, or return to Z-axis in the presence of H_0 , and T_2 is related to the phase information loss, in the precession of an ensemble of nuclei, under

the influence of local field spread. This does not amount to restoration of statistical equilibrium of the overall spin-lattice system.

Owing to this, T_1 and T_2 are termed the longitudinal and the transversal relaxation times, respectively. The assumptions in the Bloch equations have been examined by Wangsness and Bloch (1953). The details are given in Andrew [10].

The equation in the laboratory frame is,

$$\frac{d\vec{M}}{dt} = \gamma \vec{M} \times \vec{H} - \frac{M_x}{T_2} \hat{i}_x - \frac{M_y}{T_2} \hat{i}_y - \frac{(M_0 - M_z)}{T_1} \hat{i}_z$$

where $\vec{H} = H_0 \hat{i}_z + B_{1x}(t) \hat{i}_x + B_{1y}(t) \hat{i}_y$, is the resultant magnetic field, and B_{1x} , B_{1y} are the components of a circularly polarized magnetic field. $\vec{M}(t)$ describes the trajectory of the net magnetization. A detailed discussion of the Bloch equation is considered in Chapter 3.

2.4 PRINCIPLE OF NMR IMAGING

The concept of imaging using NMR follows logically from the background in the previous section.

The Larmour equation

$$\frac{d\vec{w}_0}{dt} = -\gamma \vec{H}_0$$

implies, that superposition of a spatially varying magnetic field $\vec{H}(\vec{r})$ over \vec{H}_0 , amounts to a spatial variation of the Larmour frequency,

$$\vec{\omega}_0(\vec{r}) = -\gamma (\vec{H}_0 + \vec{H}(\vec{r}))$$

The variation $\vec{\omega}_0(\vec{r})$ is linear if $\vec{H}(\vec{r})$ varies linearly over \vec{r} .

$\vec{H}(\vec{r})$ may be written as

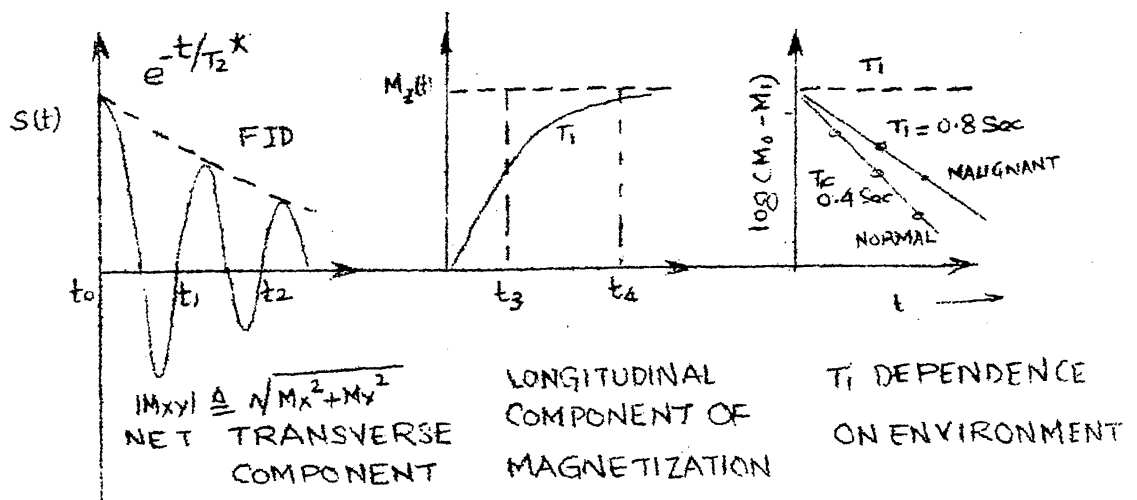
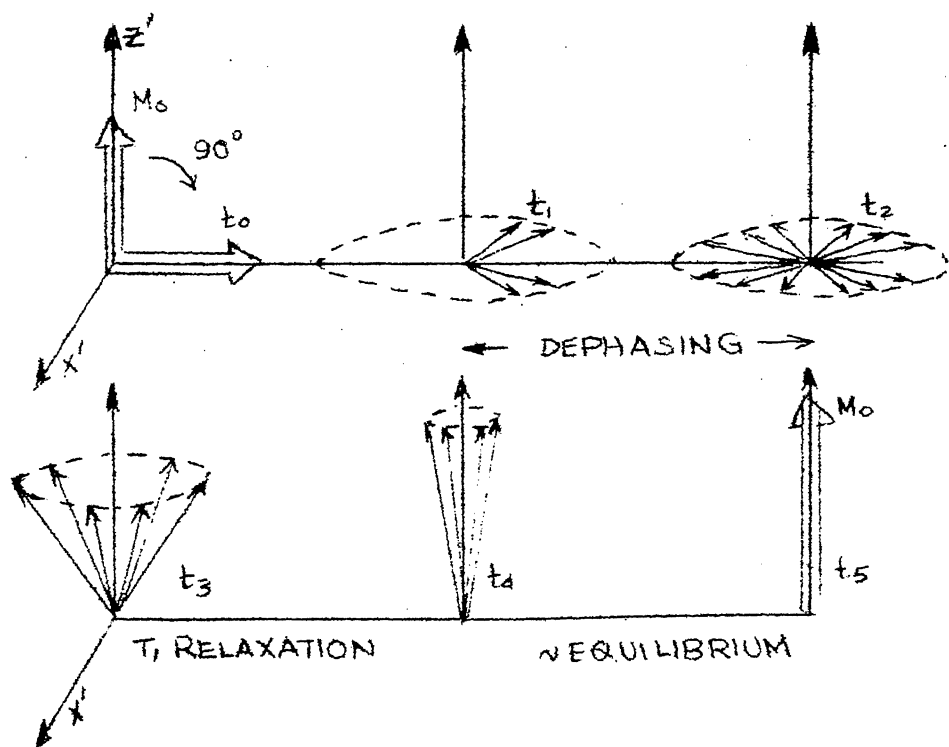
$\vec{H}(\vec{r}) = -\vec{G}(\vec{r}) \cdot \vec{r}$ where $\vec{G}(\vec{r})$ is the magnetic field gradient.

In the simple case of a field gradient in the x direction

$\vec{\omega}_0(x) = -\gamma (\vec{H}_0 + \vec{G}_x x)$, where the gradient is imposed over the main magnetic field.

Alternatively, the equation implies a mapping between the spatial coordinates, x and \vec{r} and the frequency $\omega(\vec{r})$. The primary response in NMR imaging is the distribution of the nuclear spin, usually of protons. This amounts to an image formation with the spin density distribution denoting the intensity of the image.

It may be noted that the resolution is determined by the magnitude of the magnetic field gradient $G_x(x)$ rather than the wavelength of excitation.

FIGURE 2-3b T_1 AND T_2 DEPENDENCE [6]

NMR imaging offers four parameters to be imaged, namely

$$\begin{array}{l} \rho(x,y,z), \text{ spin density} \\ \left. \begin{array}{l} T_1(x,y,z) \\ T_2(x,y,z) \end{array} \right\} \text{Relaxation times} \end{array}$$

and v , velocity of flow.

The relaxation times depend on the environment in which the spins are embedded. It has been pointed out that in clinical imaging (for the detection of lesions) relaxation specific imaging is more effective than spin density distribution [6]. Figure 2.3b, illustrates the nature of T_1 and T_2 , and the relation of T_1 , with the existence of tumours. This technique is also sensitive to velocity, the effect being similar to the doppler in the Radar context. The dependence finds use in imaging blood flow (and vessels).

2.5 A BASIC NMR EXPERIMENT

There are three basic constituents in an NMR experiment. They are

1. A steady Magnetic Field H_0 along the Z-axis defining the operating frequency w_0 .
2. A circularly polarized radio frequency magnetic field, in the transversal or x,y plane of frequency w_0 , providing the excitation.

3. The response of the sample under study.

Two modes of excitations used are the 1. CW and 2. Pulsed forms. These define the two basic modes of experimentation. They are discussed briefly below :

1. CW NMR : Early experiments in NMR were conducted in this form. A linearly polarized rf magnetic field is coupled to the sample kept in a steady magnetic field. One of the circularly polarized components interacts with the nuclear spins to excite them to a higher energy level. The coupling of the rf field is achieved with the help of a coil (e.g. solenoid), configured along with a transmitter circuit. The net absorption of energy, by the sample is detected by a change in the impedance level in the coil. Owing to a gamut of interactions in the sample (T_1 , T_2 , chemical shift and so on), the absorption is spread around the operating frequency ω_0 . Consequently, the steady magnetic field (H_0) or the rf frequency ω_0 is swept to cover the whole spectrum.

This method however has the disadvantage of long observation times, and very slow field sweeps due to the inherent insensitivity of the experiment.

2. PULSED NMR : With the advent of narrow spectral line studies in spectroscopy, CW NMR was found to be inadequate due to poor sensitivity. The pulsed method on the other hand provides the advantage of simultaneous observation of the

whole spectrum, using the NMR system's transient response. A repeated pulse excitation-observation sequence improves the sensitivity, or signal to noise ratio over the CW method for the same observation interval (Ernst and Anderson [11]). The method however requires a Fourier transformation on the transient data to obtain the spectrum. This processing is made easy in the light of the present technology.

The technique is especially useful in high resolution spectroscopy where, the magnetic field (H_0) stability requirements are stringent. The spectrum is recorded in a short time compared to the field fluctuations. Typical values of the static magnetic field (H_0) and rf field B_1 are 1 - 5 KG in imaging (and 15 - 25 KG in high resolution spectroscopy) and 1 - 10 G (peak value) respectively. The main field fluctuations (both temporal and spatial) are required to be within 1 ppm of H_0 .

The pulsed method is assumed in the rest of the thesis. The transient signal recorded is called the Free Induction Decay (FID). This is an exponential envelope (with time constant T_2) modulated over a sinusoidal carrier of frequency ω_0 . However in Imaging, when the field gradients are strong, it is seen that the decay follows a $\frac{\sin Kt}{Kt}$ behaviour, where K is determined by the gradient magnitude.

In many samples $T_2 \lesssim T_1$, a fact which is used to obtain repeated response within a single system relaxation period T_1 . The response is called a Spin Echo and is useful for expediting data acquisition in imaging. This is discussed in the next section.

2.6 SPIN ECHO :

This is a phenomenon characteristic of a pulsed NMR experiment. The concept is understood as follows :

The envelope of the FID signal decays with a time constant T_2 (where $T_2 \ll T_1$). In the classical picture this corresponds to a dephasing of the ensemble of precessing nuclei, as shown in figure 2.3b. Concurrent with the phase loss, the magnetization returns to the Z-axis alignment at a rate determined by the spin lattice relaxation. Due to relatively long T_1 , it is possible to excite the sample to reverse the dephasing into a rephasing and thus obtain a repeated FID or an echo. In pulsed experiments this rephasing is effected by a 180° Spin Echo pulse.

Two spin echo pulse sequences are illustrated in Figure 2.4. They are termed the Hahn and the CPMG sequences, and are used in pulsed NMR spectroscopy. [6]

Spin Echo may be used to find T_2 , as every rephasing occurs with a net reduction in transversal magnetization,

due to spin-spin relaxation. In NMR Imaging, this is primarily used for effective data acquisition and for obtaining $T_2(\vec{r})$ sensitive images. Additionally the FID time constant T_2^* in imaging experiments is considerably smaller than T_2 , due to increased dephasing obtained by the external gradient. An approximate expression is given as

$$\frac{1}{T_2^*} = \gamma |G(\vec{r})| L + \frac{1}{T_2} + \frac{1}{T_1} .$$

where L is the spatial extent of the sample, over which the FID is observed. Consequently another method of obtaining spin echo, is effected by using gradient reversal [12]. This is indicated in Figure 2.4. Given a gradient $G(\vec{r})$, two points in space \vec{r}_1 and \vec{r}_2 are separated in frequency by

$$\Delta \omega = \gamma G(\vec{r}) \cdot (\vec{r}_2 - \vec{r}_1)$$

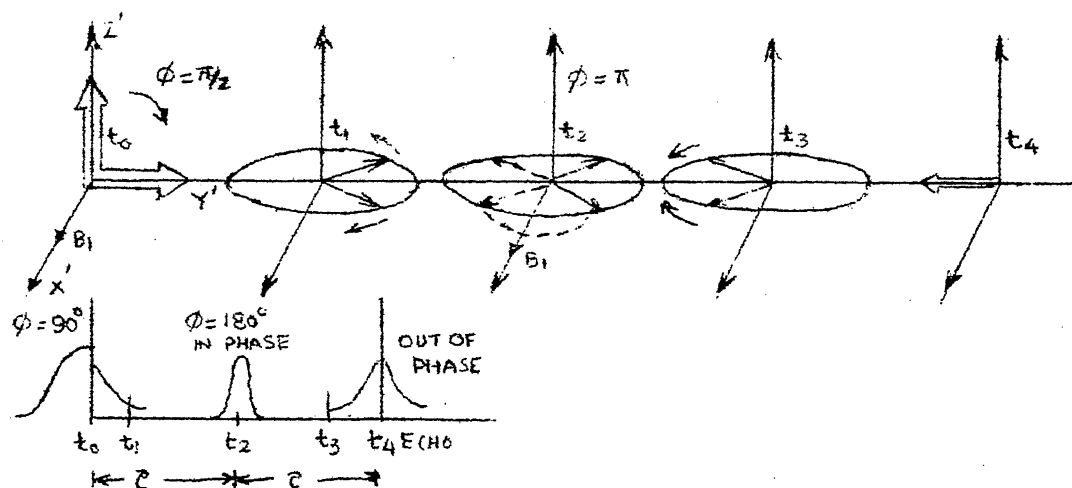
and in phase by $\Delta \phi(t) = \Delta \omega t (= \gamma G(\vec{r}_2 - \vec{r}_1) t)$.

If after time $t = T_E$, the gradient is reversed,

$$\Delta \phi(t) = \Delta \omega t = \gamma (-G(\vec{r}_2 - \vec{r}_1))(t - T_E) + \Delta \phi(T_E) \text{ for } t \geq T_E$$

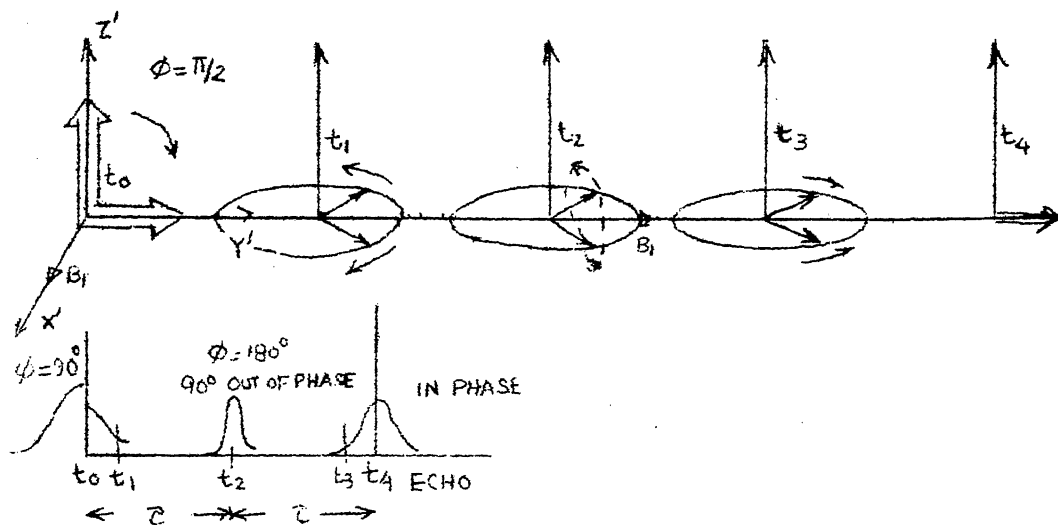
thus leading to a rephasing at time $t = 2T_E$ ($\phi(2T_E) = 0$).

It will be seen later that gradient reversal is preferred over spin echo pulses in imaging, owing to the power requirements on the transmitter.

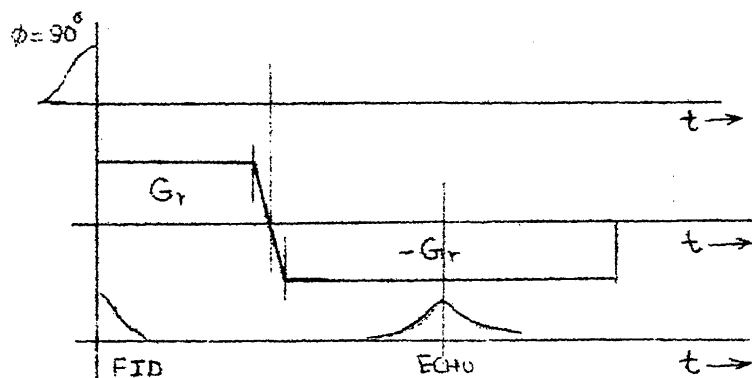


HAHN SPIN ECHO : ROTATING FRAME

EXCITATIONS ALONG X AND Y AXIS ARE 90° OUT OF PHASE



CPMG SPIN ECHO : ROTATING FRAME



GRADIENT REVERSAL SPIN ECHO

FIGURE 2.4 SPIN ECHO

2.7 IMAGING MODALITIES

NMR Imaging is marked by a variety of ways of obtaining a map of the spin density distribution, as against a fixed modality in X-ray computed tomography. The reasons for this is in the basic imaging equation itself, as will be seen in the next chapter. Heuristically the argument is based on the fact that, the field gradient in conjunction with the rf **excitation**, is capable of isolating the NMR response for a small region in space. Thus the various modalities indicate the way in which the sample responses are grouped together. Broadly the Imaging is classified into Reconstructive and Non-reconstructive methods. The former technique follows directly from the applications in CT [8], and involves reconstruction of the image in its entirety from integral projections. This method deals with ~~the~~ use of Radon transforms. Non reconstructive imaging, on the others hand is a feature characteristic of NMR. Another reason for such a classification is that, while Reconstructive schemes are marked by complexity of software processing, the latter highlights the hardware complexity.

A brief discussion of the two methods is given followed by figures, illustrating the various techniques. Tables 2.1, 2.2, list important features of each of these techniques.

1. RECONSTRUCTIVE IMAGING : This method is similar to its counterpart in CT. The procedure for extraction of the image may be understood from the basic imaging equation,

$$s(t) = \int_x \rho(x) e^{j\gamma G_x x t} dx. \quad (2.1)$$

which follows intuitively from section 2.4. A more detailed derivation is given in Chapter 3 of this thesis. The equation indicates a Fourier transformation relationship between $\rho(x)$ and $s(t)$, where

$$\rho(x) = \iint_{yz} \rho(x,y,z) dydz. \quad (2.2)$$

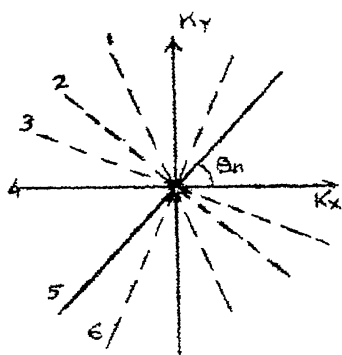
Thus $s(t)$ contains a plane-integral, (equation 2.2). The image is thus obtained by invoking the back projection algorithm, to reconstruct a 3-D or 2-D image from projections. This necessitates scanning the object space, which is also the phase space obtained by field gradients. Figure 2.5, indicates scanning of the K_x, K_y phase plane ($K_x = \gamma G_x x, K_y = \gamma G_y y$), in a radial fashion [13].

The pulse sequences for a 2-D and 3-D reconstructive imaging experiment are shown in Figure 2.6.

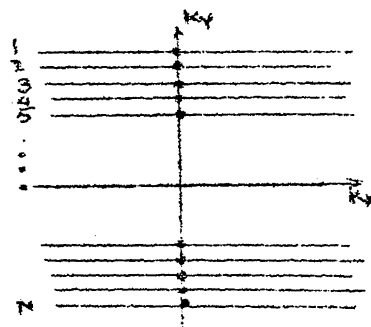
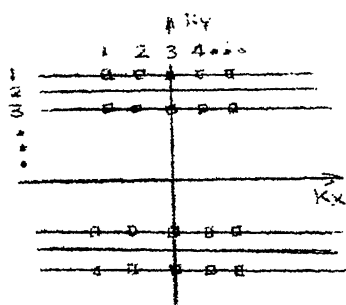
2. NON-RECONSTRUCTIVE IMAGING : All imaging modalities, which do not fall in the first category, come under this category. The sub-classifications are

- a) Point and Line Scan Imaging [14],[15],
- b) Direct fourier transform imaging [16] (DFT).

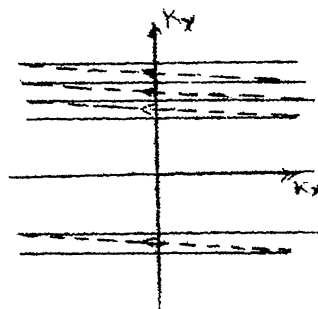
- a) Point and line scan imaging are brought about by selectively exciting a particular region of the sample i.e. a line or a point, at a time, and recording the response. This process is repeated to map the whole sample region. This procedure is marked by an involved data acquisition, though further processing is simplified. The data acquisition is also slow, which affects the net image acquisition time, an important factor in clinical applications. Figure 2.5, shows the scanning in the phase plane for 2-D imaging, while Table 2.2, lists the characteristics of the method thereof. A more detailed discussion is referred to Cho et.al., [6].
- b) Direct Fourier Transform imaging involves a line scanning of the phase plane, somewhat akin to a raster. The received data is then subject to a direct 2-D or 3-D fourier transform for image formation. The data is processed in a 2-D or 3-D form, defined by the scanning and is achieved by switching the x,y and z gradients. The method is originally due to Kumar, Welte and Ernst [16] (KWE), and is a normal mode of imaging in clinical contexts, where some modified Direct Fourier Transform methods are employed as indicated.



2-D Projection Reconstruction

Line Scan Imaging
(dots indicated line selection)

Point Scan Imaging

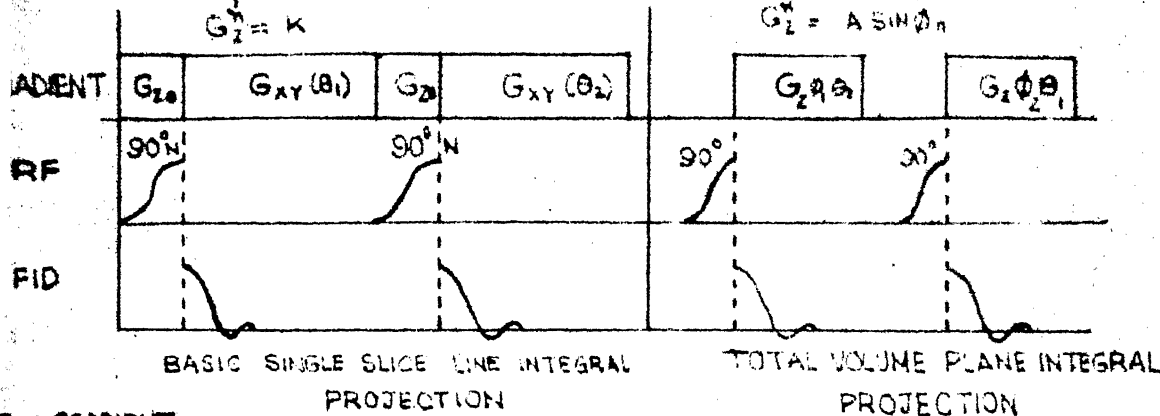


Fourier Zeugmatography

Figure 2.5 'Imaging' on the Phase Plane

$$\begin{aligned} G_x^n &= A \cos \theta_n \\ G_y^n &= A \sin \theta_n \\ G_z^n &= K \end{aligned}$$

$$\begin{aligned} G_x^n &= A \cos \theta_n \cos \phi_n \\ G_y^n &= A \cos \theta_n \sin \phi_n \\ G_z^n &= A \sin \theta_n \end{aligned}$$



GRADIENT

ROTATION ANGLE

RF : NARROW BAND

SLICE, SELECTIVE PULSE

(N)

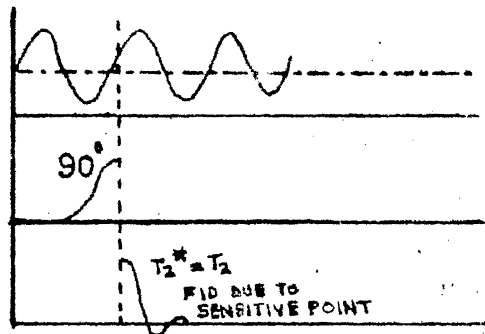
BROAD BAND PULSE

(B)

GRADIENT

RF

FID
(LOW PASS
FILTERED)



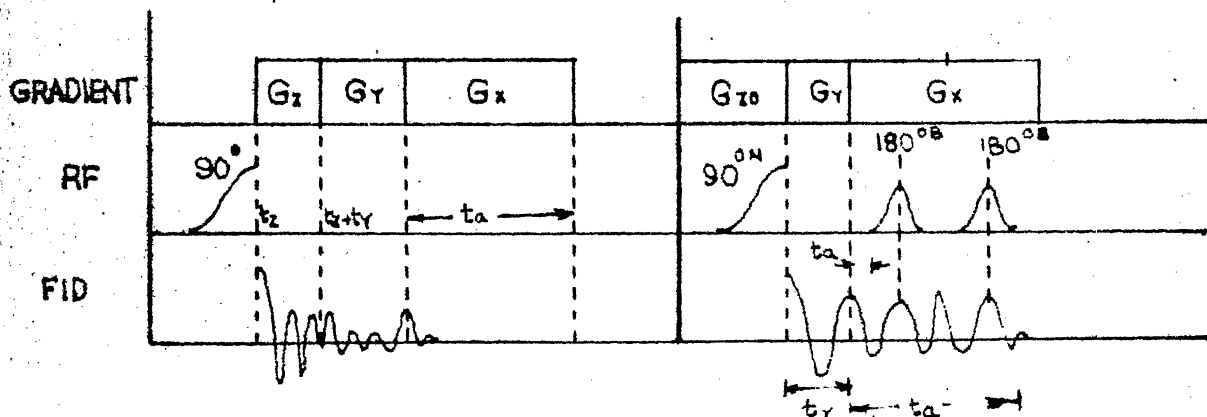
POINT SCANNING : (SELECTIVE)

SENSITIVE POINT METHOD

$$G_x = A_0(x) \sin \omega t$$

$$G_y = B_0(x) \cos \omega t$$

$$G_z = C_0(x) \sin \omega t$$



BASIC 3-D KWE
DIRECT FOURIER TRANSFORM
(CDFT)

2-D IMPROVED
KWE DFT

(FID'S (FOUR) A, B, C, D SPAN THE PLANE)

(A, B) AND (C, D) ARE CONJUGATE PAIRS

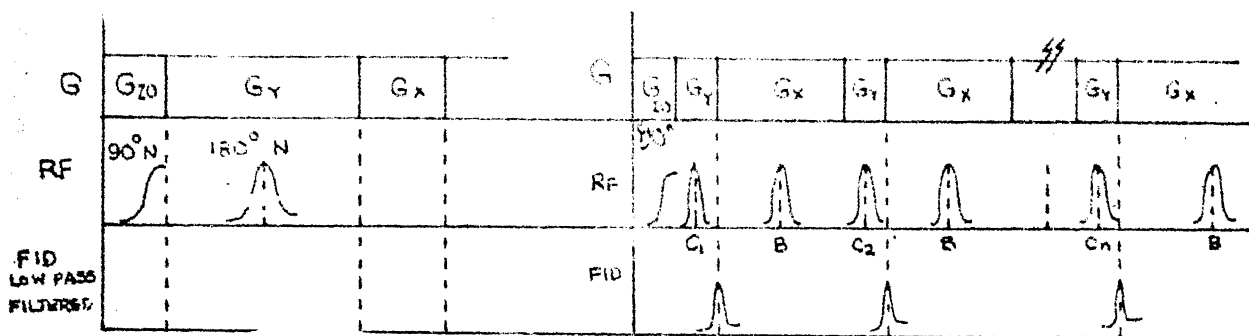
G_x READ OUT GRADIENT

G_y } GRADIENT PULSES
G_z }

G_x : READOUT GRADIENT

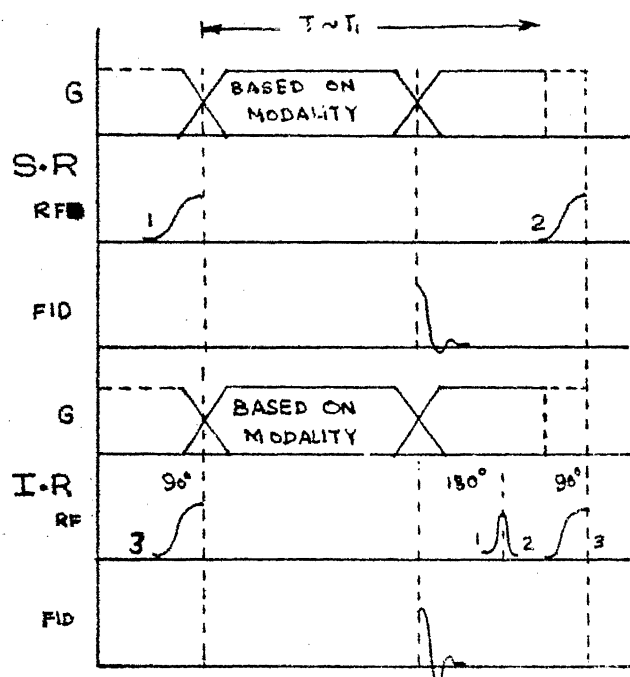
G_y : GRADIENT PULSE

G_z : SLICE SELECTION



SINGLE LINE SCANNING

MULTIPLE LINE SCANNING
(CUSES HADAMARD CODING)



N LINES OBSERVED USING
COMPOSITE PULSES

RF:

90° NARROW BAND

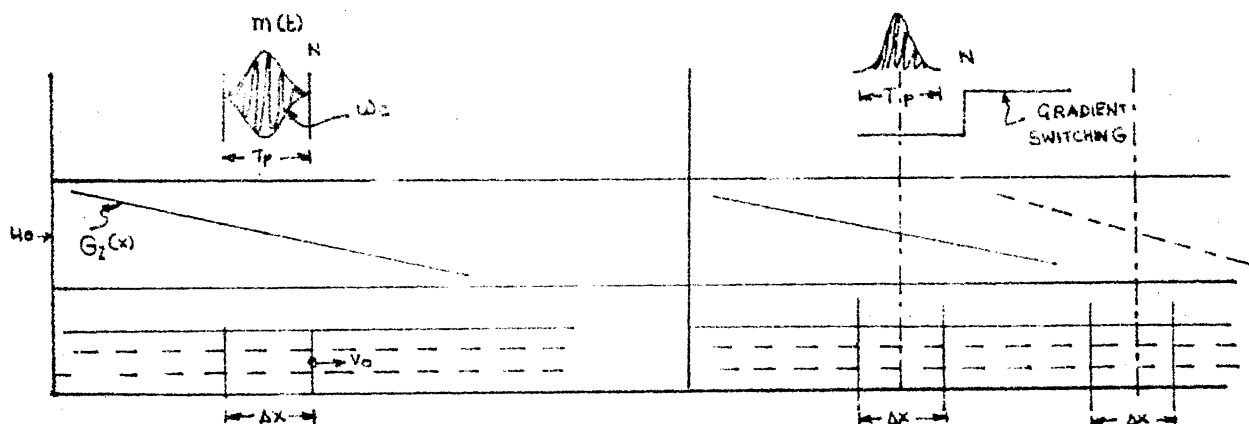
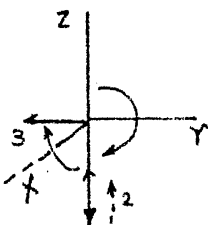
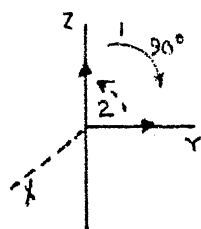
C_n 180° COMPOSITE
SELECTIVE

B 180° BROADBAND
REPHASING

COMPOSITE PULSE GENERATION
USES HADAMARD CODING

-1 0° HAHN SPIN ECHO

+1 90° CPMG SPIN ECHO



NUCLEI WITH $V_{DRIFT} < V_c$

NUCLEI WITH $V_{DRIFT} > V_c$

$V_c \equiv \frac{\Delta x}{T_p}$ IS THE
CRITICAL VELOCITY
DOPPLER IMAGING

TABLE 2.1

RECONSTRUCTIVE IMAGING

Modality Parameters	Basic Single Line Integral Projection (2D)	Total Volume Plane Integral Projection
Gradient Sequence	$G_{zo} \rightarrow G_{xy}$ Slice Readout Selection	$G_z((\phi_n), \theta_m)$ Readout
Elementary rf Excitations	Narrowband 90° Pulse	90° Rectangular Pulse
Basic Exci- tation Sequ- ence Timing	T_p : Pulse Duration T_s : Aquisition Time	T_p : Pulse Duration
Spin Echo	None	
Detection and Filtering	Quadrature and Antialiasing filter	
Time for One Sequence	$T_p + T_s$	$T_p + T_s$
Repetition Time :		
Spin Density SR/IR	$\frac{T_1}{T_1}$	$\frac{T_1}{T_1}$
Time for Total Experiment	For M Projections MT_1	MT_1
Signal Avg. gain for Basic Sequence	1	1
Number of computations	$\leftarrow \text{M Projections and N Points} \rightarrow$ $MN(\log_2 N+1)$	
Image Resolu- tion Dependence Modalitywise	Mem $N(\log_2 N+1)$ Mem $= M$ 1. Choice of the deconvolution Kernal or the de-blurring function [6], [8]. 2. Number of Projections M 3. SNR	

* Method marked by simple data acquisition, computational complexity and SNR degradation due to blurring.

TABLE 2.2 FOR RECONSTRUCTIVE IMAGING

Modality Parameters of the Tech.	Single Line	Line Scanning Multiple Line	Multiple Slices
Elementary rf Excitations	Narrow Band 90° Pulse Narrow Band 180° Spin Echo Pulse	Narrow Band 90° Pulse Composite (Frequency and Phase) 180° Pulse Broad Band 180° Re-phasing Pulse	Composite 90° Pulse for Multi Slice Selection Broad Band 180° Re-phasing pulse or Gradient Reversal
Gradient Sequence	$G_{z0} \rightarrow G_{y0} \rightarrow G_{x0}$ Selects Gradient Readout Pulse Single FID Slice Selects	$G_{z0} \rightarrow G_{y0} \rightarrow G_{x0}$ Selects Selects Selects Line Composite FID FID	$G_{z0} \rightarrow G_{y0} \rightarrow G_{x0}$ Readout Selects Selects Lines Composite FID
Basic Excitation Sequence Timing	T_p : Pulse Duration T_e : Echo Time T_s : Acquisition	Same as single line	Same as single line
Spin Echo	Hahn Readout Data Acquisition in one Relaxation	Hahn - Readout composite Readout composite CPMG Data Acquisition	Hahn and CPMG - Composite Hahn - Broadband
FID Detection & Filtering	For M Lines $M(2T_p + 2T_R + T_s)$ Time for one Seq.	Quadrature Detection and Acquisition Filter For M Lines $(M+1)T_p + 2MT_R + MT_s$	For P Slices and M Lines $P(M+1)T_p + 2PM_T + PM_T s$
Repetition Spin Time T_1	T_1 Assuming M Points per line $(M(M \log_2 M) M(2-D FFT_s))$	Time for one sequence if less than T_1	same as single line
Number of Computation			
Time for Total Experiment	$< MT_s$ for Saturation/Inversion Recovery, Less otherwise		
Signal Avg. Gain for Basic Sequence	1	$(M)^{1/2}$	$(PM)^{1/2}$
Image Resolution	1. Narrow Band 180° Pulse	1. Composite 180° Pulse	
Dependence Modality Features	2. SNR 1. Biased Towards Hardware 2. Fast Acquisition 3. Easy offline processing	2. SNR 4. Switched Gradients 5. Required proper pulse tailoring in frequency and phase.	7. Signal averaging Gain > 1

TABLE 2.2 continued

Modality Parameters of the Technique	Point Scanning	Direct Fourier Transform (3D) and (2D)	Fourier Transform or Fourier Zeugmatography Improved DFT
Elementary RF Excitations	900 (Rectangular)	900 (Rectangular) narrow band or composite, 900 pulse	narrow band or composite, 900 pulse Broadband 1800 pulse or Gradient reversal
Gradient Sequence	$G(x)=A(x)$ $G(y)=B(y)$ $G(z)=C(z)$	$\sin \omega t$: Full pc $\sin \omega t$: x0 or z. $\sin \omega t$: such that, $A(x_0)=0$ $B(y_0)=0$ $C(z_0)=0$	$G_z \rightarrow G_y \rightarrow G_x$ Slice selection
Basic Excitation	T_p : Pulse duration	T_p : Pulse duration	T_p : Pulse duration
Sequence timing	T_s : Acquisition	T_p : Z Gradient duration T_y : Y Gradient duration T_s : Acquisition	T_p : Z Gradient duration T_y : Acquisition of one FID T_s : Total Acquisition
Spin echo	None	Hahn	CPMG
FID Detection	Phase sensitive detection		
Filtering	Antialiasing Filter		
Time for one Seq.	For N Points $N(T_s)$	For $M \times M \times M$ data set (3-D) $M^2 T_p + M^2 T_s + \sum_{i=1}^M \Delta T$	
Repetition Spin density	T_1		
Time	T_1 Specific using EX/IR		
Number of Computations	None	For 2-D $M^2(M \log_2 M)$	For 2-D $M^2(M \log_2 M)$
Time for Experiment	$M^2 T_1$	$M^2 T_1$	$M^2 T_1$
Single averaging gain	1	1	1
for basic sequence	1. Stability of $A(x), B(x), C(x)$		
Image resolution	2. Residual FI after filtering		
dependence modality	3. SNR		
wise			
Features	1. Complicated hardware 2. Time varying gradients 3. Slow, due to large spin lattice Relaxation time T_1	1. Simple hardware 2. Fast acquisition 3. Longer computation times 4. Switched gradients 5. T_1 contrast imaging possible	1. SLICE THICKNESS 2. SNR

3. RECOVERY SEQUENCES : T_1 SENSITIVE IMAGING

This sequence essentially imposes a condition on the repetition time of the read sequence, followed by a modality. The rationale is that, subsequent to a 90° pulse, applied for maximizing the FID response, the spin lattice relaxation mechanism sets in, which tends to return the magnetization to the Z axis. As a result, another 90° pulse applied at time $T_R = T_1$, of the first pulse would evoke a different response. Successive repetitions lead to a steady state response, dependent on the repetition time T_R . Optimum repetition time T_R is found to be near T_1 . In its basic form, the sequence is termed Saturation Recovery (SR), and is illustrated in figure 2.6. The exact dependence on T_1 is derived in Chapter 3 of the thesis. The method is employed to obtain T_1 dependent images, which are known to give good results in lesion detection, as shown in Figure 2.3b.

A modification of this is the Inversion Recovery (IR) sequence shown in Figure 2.6. This includes a 180° pulse, following the FID read out, amounting to an increased T_1 dependence, and is seen to give better contrast. Heuristically, the dependence is owing to a phase inversion in alternate read sequences. It may be stated that Saturation and Inversion recovery sequences are not modalities per se, but are used in conjunction with them to elicit the T_1 dependence.

4. SPIN ECHO IMAGING (SE) :

Applications involving a strong dependence on spin-spin relaxation time T_2 , employ this method. Control over the echo time T_E ($\sim T_2$), obtains a response dependent on $T_2(x)$. The response is weighted by a factor $e^{-T_E/T_2(x)}$ will be seen in the next chapter.

5. DOPPLER IMAGING :

In clinical context NMR has been used for imaging blood vessels by exploiting this peculiar dependence. Figure 2.6 illustrates the phenomenon. A selective excitation of a small region of the sample of extent Δx for a duration T_p , extracts a response from the sample due to those nuclei, whose net outward drift velocity is less than $\Delta x / t_p$. Thus excess motion may be filtered out at the detection level, to avoid motion artifacts.

Nuclei with velocities greater than $\Delta x / t_p$ may also be imaged by receiving the signal from regions adjacent to the excited sample volume by applying an appropriate field gradient. A detailed discussion of such selective imaging techniques is given by Macovski [4]. To sum up, the potential of NMR imaging lies in the four parameters ρ , T_1 , T_2 and V , which highlights various aspects of an image.

2.8 EXCITATIONS IN IMAGING :

To aid the understanding of the figure 2.6 , a discussion of some salient excitation pulses, follows :

1. rf PULSES : The rotating rf magnetic field is tailored to stimulate either the whole sample or specific regions. Consequently there are :

a : 90° and 180° Broad Band Pulses :-

The spectra of these pulses are broad and are designed to ~~excite~~ the whole sample in the presence of strong field gradients. The power requirements on these pulses are large and are therefore used sparingly in imaging experiments. In most imaging techniques 90° pulses, initiate a sequence, and may be applied before imposing the gradients, thereby obviating the necessity for the broad band stimulus. However, broad band 180° pulses are used for producing spin echo, in the middle of a pulse sequence. Sometimes gradient reversal is also employed for generating spin echo, though the method is constrained by switching speed.

b : 90° and 180° Narrow Band Pulses :

These excitations are used to selectively stimulate a region of the sample, and are important in non-reconstructive modalities. They are employed to effect slice selections in 2D-DFT Imaging and in selective line and point scanning

procedures. The choice of pulse shaping is complicated by the nonlinear nature of NMR, and the problem is addressed to in Chapter 3 of the thesis. It may be noted that in certain instances image resolution is governed by pulse selection.

2) FIELD GRADIENTS : Two types of gradients are used in Imaging, they are :

a : Read Out Gradient : This is a constant gradient applied in a particular direction, usually along the x axis for a duration $T \gg 1/\gamma G_x L$. The purpose is to effect the read out of the response, and is used in line scan and direct fourier transform imaging.

b : Gradient Pulse : It alludes to the case where the duration of the gradient is shorter than the dephasing time $1/\gamma G_x L$, so that the transverse magnetization remains in phase, while being modified marginally by the pulse. Its use is in Direct Fourier Transform or Fourier Zeugmatography.

CHAPTER 3

MATHEMATICAL MODEL OF THE NMR IMAGING SYSTEM

3.1 REQUIREMENTS OF THE MATHEMATICAL MODEL : NMR AS A SYSTEM IDENTIFICATION PROBLEM

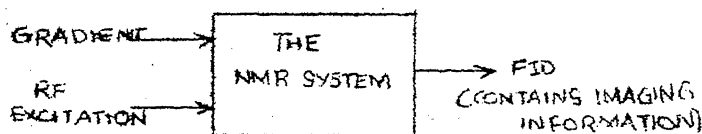
The use of NMR as an imaging technique is already a decade old, and the method has seen the evolution and development of various modalities within the main framework of NMR. A review of these modalities were presented in Chapter 2. However with the requirements of full scale systems, to cater to a variety of applications in clinical and chemical contexts, it becomes necessary to unify, or at least to identify common points underlying the various modalities. Any meaningful comparison of the imaging method, from the system point of view, would necessitate the development of a mathematical model of the processes governing the technique. In NMR a good starting point is the Bloch equations, covered in chapter 2 of the thesis. However it will be seen that the nonlinear nature of the equations has been a barrier in developing simple quantitative models to describe the response, especially to arbitrary excitation pulses. The recent past has seen work in mathematical description of NMR imaging, Hoult [17], Mansfield and Maudsley [18] and Caprihan [19].

Before starting the discussion of the mathematical model, the requirements on NMR as a system identification problem is examined. The four parameters in this method are

$\rho(\vec{r}^>)$, $T_1(\vec{r}^>)$, $T_2(\vec{r}^>)$ and v . The mapping of the spatial information to the frequency spectrum is obtained by the application of a magnetic field gradient in any general direction $\vec{r}^>$ (the field itself being aligned with $\vec{H}_0^>$). Consequently, considering the NMR system (with the sample under study) as a black box, the inputs are, 1. The field gradient $\vec{G}(\vec{r}^>)$ and 2. The rf excitation $B_1(t)$ while the output is the FID $s(t)$. The main magnetic field $\vec{H}_0^>$ defines the operating frequency of the experiment, and is not presented as an input, since some form of demodulation or frequency translation is inherently assumed. Figure 3.1, describes schematically the systems approach. The following observations may be made at the outset, before commencing an analysis with the Bloch equations.

They are

1. The relationship between the input and output is involved, due to the nonlinearity of the Bloch equations.
2. The system is multi-input and single-output, a fact to be borne out by the model to be developed.
3. Any linearity in the system is not obvious on a cursory examination.
4. The system response, namely the FID is observed after the cessation of the rf pulse. This constraint is imposed by practical considerations, namely that the transmitted power is



large compared with the NMR response, thus swamping out the receiver.

3.2 BLOCH EQUATIONS (Details in the Rotating Frame of Reference in the Presence of Field Gradients) :

The section 2.3 presents the phenomenological model due to Bloch. The rationale and assumptions involved therein are indicated. The vector dynamical equation of magnetization \vec{M} (assuming a lumped model) is given by

$$\frac{d\vec{M}}{dt} = \gamma \vec{M} \times \vec{H} - \frac{M_x}{T_2} \hat{i}_x - \frac{M_y}{T_2} \hat{i}_y - \frac{(M_z - M_0)}{T_1} \hat{i}_z \quad (3.1)$$

where $\vec{H} = H_0 \hat{i}_z + B_{1x}(t) \hat{i}_x + B_{1y}(t) \hat{i}_y$, is the resultant magnetic field.

In this equation, the first term $\vec{M} \times \vec{H}$ is due to the interaction of the net magnetization with the resultant magnetic field, while the remaining terms are included phenomenologically. These are a set of three scalar equations, determining the trajectory of the x, y and z components of the magnetization \vec{M} .

In the case of field gradients being applied to the main field, it is more convenient to treat the Bloch equations in the rotating frame of reference, as explained in Chapter 2. The parameters of the reference frame are as follows :

1. The rotating frame is labelled X' , Y' and Z' .

2. The rotation frequency ω_0 is the Larmour frequency given by $\omega_0 = \gamma H_0$. The direction of the corresponding vector \vec{w}_0 is opposite in sense to \vec{H}_0 .

3. The residual field due to the field gradient, at location \vec{r} is denoted by $\Delta H(\vec{r})$.

4. The rf excitation $B_1(t)$ has a frequency ω_0 .

Hence the vector equation in the rotating frame is

$$\frac{d\vec{M}_R}{dt} = \vec{M}_R \times \vec{H}^* - \frac{M_X}{T_2} \hat{i}_X - \frac{M_Y}{T_2} \hat{i}_Y - \frac{(M_Z - M_0)}{T_1} \hat{i}_Z, \quad (3.2)$$

where $\vec{H}^* = \Delta H(\vec{r}) \hat{i}_Z + B_1(t) \hat{i}_X + 0 \cdot \hat{i}_Y$

(obtained by choosing the X' -axis along the $B_1(t)$ phasor)

and $\vec{M}_R \triangleq M_X \hat{i}_X + M_Y \hat{i}_Y + M_Z \hat{i}_Z$, all components being functions of time(t) and position \vec{r} (w.r.t. the laboratory frame). Writing the three components separately yields

$$\frac{dM_X}{dt} = \gamma(\Delta H M_Y - \frac{M_X}{T_2})$$

$$\frac{dM_y'}{dt} = \gamma B_1(t) M_z' - \gamma(\Delta H) M_x' - \frac{M_y'}{T_2} \quad (3.3)$$

$$\frac{dM_z'}{dt} = -\gamma B_1(t) M_y' - \frac{(M_z' - M_0)}{T_1}$$

Defining M as

$$M \triangleq M_x' - j M_y'$$

(since orthogonal components in the transverse plane of the rotating coordinates has a quadrature phase relationship in the laboratory-frame), the Bloch equations simplify as

$$\frac{dM}{dt} + \left(\frac{1}{T_2} - j \gamma \Delta H(\vec{r})\right) M = -j \gamma B_1(t) M_z' \quad (3.4)$$

$$\frac{dM_z'}{dt} = \gamma B_1(t) \text{Im } M - \frac{(M_z' - M_0)}{T_1}$$

The term corresponding to T_1 may be neglected for all $t \ll T_1$. It may be noted that the Bloch equations are written for a spatial location \vec{r} in the sample, so that M_x' , M_y' , M_z' , T_1' and T_2' are functions of \vec{r} (the location in the laboratory frame).

The NMR response is observed in the $X'Y'$ plane, and consequently $M(t)$ is the variable of interest. These equations are coupled, and the nonlinearity is imposed through the time varying rf field envelope $B(t)$, which appears as a coefficient in the differential equations. When $B_1(t) = 0$, a situation which arises on the cessation of the excitation, the evolution of the magnetization M is governed by linear differential equations. Therefore the FID signal may be thought of as the output of a linear system, whose initial conditions are related nonlinearly with $B_1(t)$. This fact is brought out more clearly from the geometrical arguments to be presented in section 3.3.

A solution of Bloch equations(3.3), in the presence of $B_1(t)$ and field gradient $\Delta H(\vec{r})$, is reviewed in section 3.4. The problem is especially relevant in rf pulse tailoring for narrow band selective excitations.

3.3 THE BASIC NMR IMAGING EQUATION (From geometrical arguments in the rotating frame of reference) :

A **rigorous** solution of the NMR imaging problem lies with the Bloch equations, in spite of the model being based on macroscopic phenomena. However, it is possible to gain useful insight into the imaging equation, by considering the

geometrical argument of the precessing magnetization. The object of the present section is to show that the imaging equation may be arrived at from rotating frame arguments.

The following assumptions are used in the derivation of the equation :

1. The Larmour equation $\vec{w} = -\gamma \vec{H}$ is valid during the pulse duration T_p . i.e., system transient times are very small compared to T_p .
2. The pulse duration $T_p \ll T_1, T_2$.
3. The modulating envelope $B_1(t)$ is rectangular.

For the sake of simplicity, the case of a single direction gradient, $\vec{G}(x)$ in the x-direction is considered. The symbols to be used in the discussion are

$M_0(x)$ - The equilibrium magnetization in the interval Δx around x .

$\rho(x)$ - One dimensional spin density distribution

$$\rho(x) \triangleq \int_Y \int_Z F(x, y, z) dy dz$$

A - : The cross sectional area of the sample.

Figure 3.2, illustrates the precession of the resultant magnetization. The precession cone is indicated by broken lines in the

figure. The cone degenerates to a circle at $x = 0$ where $\Delta H(x) = 0$. The associated equations are,

$$\bar{B}_{\text{res}}^> = ((\Delta H)^2 + (B_1)^2)^{\frac{1}{2}}$$

$$\tan \theta = B_1 / \Delta H = B_1 / G_x x$$

$$\phi = \gamma \left| \bar{B}_{\text{res}}^> \right| T_p \text{ is the flip angle.}$$

At time T_p , the magnetization has the orientation determined by ϕ , θ and $M_0(x)$, the length of the magnetization. The X and Y components of the magnetization M_x and M_y respectively are projections of $M_0(x)$. After the cessation of the rectangular pulse, the magnetization precesses freely about the Z axis at a rate $\Delta \omega = \gamma \Delta H(x)$. Hence

$$M_x'(x) = M_0(x) F_x'(x)$$

$$\text{and } M_y'(x) = M_0(x) F_y'(x)$$

where $F_x'(x)$ and $F_y'(x)$ are projections of $M_0(x)$ at time T_p . writing $M(x)$ as

$$M(x) = M_x'(x) - j M_y'(x),$$

$$\text{or } F(x) = F_x'(x) - j F_y'(x).$$

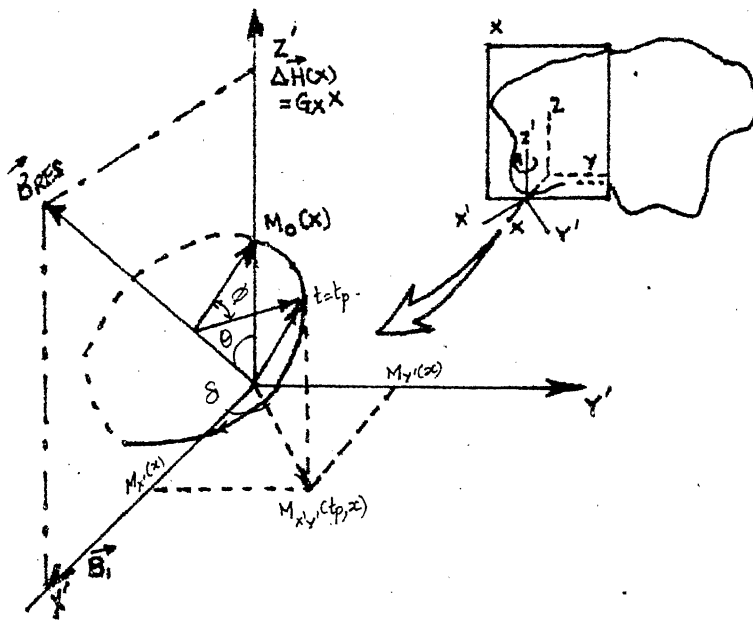


FIGURE 3.2 ROTATING FRAME
AT POINT X

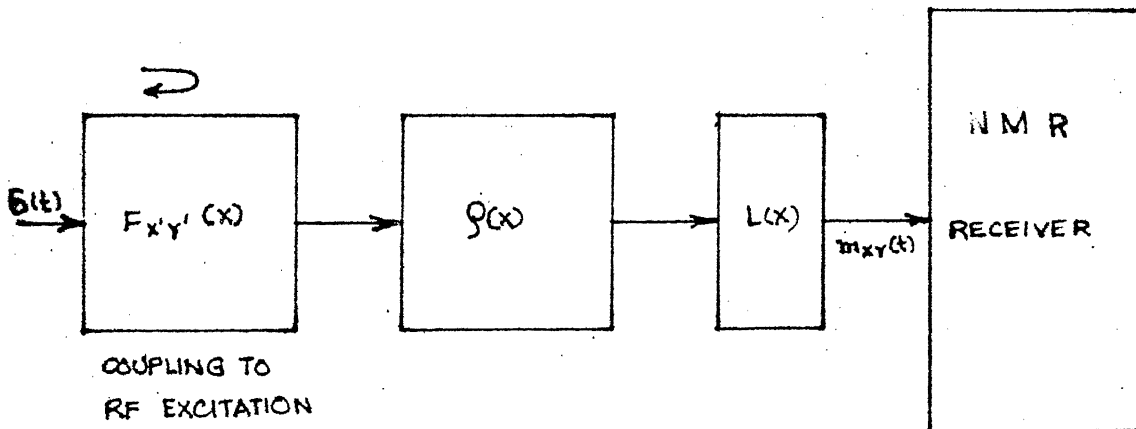


FIGURE 3.3 NMR IMAGING SYSTEM

the magnetization $M_0(x)$ in turn may be expressed as

$$M_0(x) = K \rho(x)$$

where K is a constant of proportionality relating spin density to magnetization.

At the end of the pulse duration

$$M_{x'y'}(x) = K F_{x'y'}(x) \rho(x)$$

The subscripts indicate that the phasors M and F are in the $x'y'$ plane, and is implicitly assumed hereafter.

The future evolution of the magnetization is determined by the field gradient $\Delta H = G_x x$. Thus,

$$M(t) = K F(x) \rho(x) e^{j \gamma G_x x t}$$

The aggregate response from the whole sample is the magnetic moment,

$$m(t) = KA \int_x F(x) \rho(x) e^{j \gamma G_x x t} dx \quad (3.5)$$

The derivation neglects the effect of T_2 and T_1 on the assumption that $T_{p.m.} \ll T_1, T_2$ which is not valid for the longterm evolution of the magnetization. Its first order effect (when $\frac{1}{G_x L} \ll T_2$) is a multiplicative term, $e^{-t/T_2} f(T_1)$.

Therefore the response $m(t)$ is given by

$$m(t) = KA \left(\int_x F(x) \varphi(x) e^{j\gamma_g x t} dx \right) e^{-t/T_2} f(T_1) \quad (3.6)$$

This expression is cast in the form of the Fourier transformation, and is the basic NMR equation. The term $F(x)$ serves as an aperture function, which modifies the effect of $\varphi(x)$.

In the case of the rectangular pulse,

$$F(x) = \sin \theta \cos \theta (1 - \cos \phi) - j \sin \theta \sin \phi.$$

while the expression is fairly complex in the case of arbitrary pulse excitations. A more detailed discussion is presented in appendix A.

The imaging equation suggests the following :

1. The response $m(t)$ is linearly related to $\varphi(x)$, the system identification function,
2. The aperture function $F(x)$ is nonlinearly related to the rf excitation $B_1(t)$.

This is the nonlinearity referred to in the Bloch equations. As a result the solution of Bloch equations are necessitated to determine $F(x)$ or the design of the pulse $B_1(t)$ to obtain a specific form for $F(x)$. This problem is

important in selective excitations, where the resolution of the image is determined by the aperture function.

More generally, when the effect of the relaxation are spatially dependent, the behaviour is no longer exponential. The resultant transverse magnetic moment $m(t)$ is

$$m(t) = KA \int_{x_s} F(x) \rho(x) L(x) e^{j\gamma G_x x t} dx \quad (3.7)$$

where the function $L(x)$, accounts for the effect of the relaxation phenomena.

This equation may be interpreted in terms of transfer functions, where $\rho(x)$ and $L(x)$ define the system parameters to be identified, and $m(t)$ may be treated as the impulse response of the transfer function $F(x) \rho(x) L(x)$ as shown in Figure 3.3.

The imaging equations may also be derived directly from the Bloch equations and is given by Hinshaw [20].

The generalization to three dimensions yields

$$m(t) = K \int_{V_s} F(\vec{r}) \rho(\vec{r}) L(\vec{r}, t) e^{j\gamma [\vec{G}(\vec{r}) \cdot \vec{r}] t} dV. \quad (3.8)$$

3.4 A SOLUTION OF THE BLOCH EQUATIONS (perturbation technique due to Hoult)

Sections 3.2 and 3.3 indicate the formulation of the Bloch equations in the rotating frame of reference, and the derivation of the basic imaging equation (3.6), identifies the aperture $F(x)$ with the nonlinear component of the Bloch equations.

For the rectangular pulse, $F(x)$ is given as

$$F_y'(x) = \gamma B_1 T_p \operatorname{sinc} \left(\frac{B_{\text{res}}}{B_1} \cdot \pi/2 \right)$$

and

$$F_x'(x) = \frac{B_1 G_x x}{(B_1^2 + (G_x x)^2)} \left(1 - \cos \frac{B_{\text{res}}}{B_1} \pi/2 \right) \quad (3.9)$$

for a 90° flip. The solution for arbitrary excitations may be obtained numerically using a piece-wise rectangular approximation in the rotating frame (Caprihan [19]). It is shown that gaussian, sinc and triangular modulations are good excitations, though not optimum. A more rigorous analytical solution is attempted by Silver et al., [21]. However Hoult's perturbation solution [17], gives an insight into the nature of the equation. The magnetization $M(t)$ and $M_z(t)$ are written as a series of perturbation terms of order $\gamma B_1(t)$,

$$M(t) = M^{(0)} + M^{(1)} + \dots \quad (3.10)$$

$$M_z(t) = M_z^{(0)} + M_z^{(1)} + \dots$$

Doc. No. A 00221

then as perturbation terms, $M^{(n)}$ and $M_z^{(n)}$, the Bloch equations yield

$$\begin{aligned} \frac{dM^{(n)}}{dt} + \left(\frac{1}{T_2} - j\gamma H(\bar{r}^>) \right) M^{(n)} &= -j\gamma B_1(t) M_z^{(n-1)} \\ \frac{dM_z^{(n)}}{dt} &= \gamma B_1(t) \text{Im } M^{(n-1)} \end{aligned} \quad (3.11)$$

with the initial conditions $M^{(0)} = 0$ and $M_z^{(0)} = M_0(\bar{r}^>)$, while the effect of T_1 is neglected.

These equations are recursive, the higher order terms being determined by successively lower order terms. The equations for the first few orders is given below,

$$\frac{dM^{(1)}}{dt} + \left(\frac{1}{T_2} - j\gamma H(\bar{r}^>) \right) M^{(1)} = -j\gamma B_1(t) M_0,$$

$$M_z^{(1)} = 0,$$

$$\Rightarrow M^{(2)} = 0,$$

and
$$\frac{dM_z^{(2)}}{dt} = \gamma B_1(t) \text{Im } M^{(1)}(t)$$

or
$$M_z^{(2)} = \int_{-\infty}^t \gamma B_1(t) \text{Im } M^{(1)}(t) dt. \quad (3.12)$$

At \vec{r}_0 , where $\Delta H(\vec{r}_0) = 0$, the magnetization M_0 precesses about $B_1(t)$ or the X' -axis. The flip angle for this case is given by $\phi = \gamma B_1 T_p$. As the effect of the perturbation term is in the product $B_1 T_p$ (or in B_1 for a given T_p) the flip angle ϕ may be treated as an indicator of the nonlinearity.

The following observations may be made from the perturbation equations :

1. The equation governing $M^{(1)}$ is linear, and is pre-dominant for smaller flip angles.
2. At flip angles such as 90° , the transversal response is nonlinear, though the magnitude of the corresponding magnetization is maximum.
3. Operation in the linear region has the advantage of easy signal design as $F(x) = \mathcal{F}(B_1(t))$, where \mathcal{F} denotes fourier transformation.
4. In the presence of a strong linear gradient, the magnetization $M^{(1)}$ at time T_p is negligible, and may be observed only with a spin echo pulse. This is due to quick dephasing by the gradients.
5. Spin echo should be employed to observe the complete response in the selective excitation case, even if a large flip angle is employed, as the primary response is linear.

6. The excitation should not possess sharp edges. This increases side lobe power in the primary response, which reduces selectivity.

7. Higher order terms of $F(x)$ ($\sim M(x, T_p)$) bear no resemblance with the spectrum of the pulse.

The latter observations are based on the assumption that the linear response $M^{(1)}$ is significant. Hoult [17] indicates a ratio for a rectangular pulse

$$\frac{M^{(3)}(T_p)}{M^{(1)}(T_p)} = -\gamma^2 \frac{B_1^2 T_p^2}{8} = -\frac{\phi^2}{8}$$

which for $\phi = \pi/2$ is 31%.

A comparison of the Bloch equations with the geometrical interpretation is given in appendix A.

Practical considerations for signal design are given by Carpihan [19]. Selection of an excitation is based on the behaviour of $F(x)$. The various parameters describing the figure of merit on $F(x)$, for selective excitations is shown in Figure 3.4 (P.62).

3.5 SYSTEM EQUATIONS FOR DIFFERENT ELEMENTARY EXCITATIONS:

The generalized imaging equation (3.8), describes the response of the NMR system to a single **rf** pulse. The function $F(\vec{r})$ may be obtained as a solution to the Bloch equations. The present sections formulates the equation for different basic excitations. They are,

1. The rf Pulses :

- a. 90° and 180° broadband
- b. 90° and 180° narrowband

2. Gradients

- a. Readout gradient
- b. Gradient pulse
- c. Gradient reversal,

all of which are treated in sections 2.6 and 2.7. Whereas the rf pulses, affect the response $M(t)$ through the aperture function $F(\vec{r})$, the gradients modify the response through the phase term $e^{j\gamma \vec{G}(\vec{r}) \cdot \vec{r}}$. It may be observed that the image resolution is affected by both functions, though primarily by the gradient. The equations of the excitations follow:

1.a 90° and 180° Broadband Pulses :

This corresponds to $F(\vec{r})$ being a constant over the sample space. Geometrically, this implies, $B_1 \gg G_x L$, $T_p \ll T_2$,

T_1 and $1/\gamma G_x L$ and $F(\vec{r}) = -j$, resulting in

$$s(t) = K \int_V \rho(\vec{r}) e^{-j\pi/2} e^{j\gamma G(\vec{r}) \cdot \vec{r} t} dV \quad (3.13)$$

1.b 90° and 180° narrow band pulses :

The pulses are primarily designed for slice selection. The general condition on $F(\vec{r})$ is shown in Figure 3.4. This corresponds to

$$B_1 \approx G_x x \text{ for } x < L, T_p \ll T_1, T_2 \text{ and } T_p \approx \frac{1}{\gamma G_x L}$$

and a proper choice of $B_1(t)$. For rectangular pulses, $F(x)$ (for a single direction) is shown in section 3.2, and the requisite pulse duration is given by the equation,

$$\text{sinc}(\gamma(B_1^2 + (G_x x)^2)^{\frac{1}{2}} T_p) = \frac{1}{\sqrt{2}\pi} \text{ for a } \pi \text{ pulse} \quad (3.14)$$

2.a Readout Gradient :

This is applied following a non-selective **rf** pulse, to effect the readout of the FID. The imaging equation is

$$m(t) = K \int_{V_s} \rho(\vec{r}) F(\vec{r}) L(\vec{r}) e^{j\gamma \vec{G}(\vec{r}) \cdot \vec{r} t} dV \quad (3.15)$$

similar to equation (3.8). It is essentially a free evolution of the magnetic moment, in the absence of an excitation.

2.b Gradient Pulse :

The duration of the pulse is shorter than $1/\gamma G_x L$, so that the magnetic moment is constant over the interval τ and

$$m(t) = K \int_{V_s} \rho(\vec{r}) e^{j(\gamma \vec{G}(\vec{r}) \cdot \vec{r})\tau} dV. \quad (3.16)$$

This is the key equation for **Fourier Zeugmatography**.

2.c Gradient reversal :

Broadband spin echo may be obtained using these pulses. The gradient $G(x)$ (in the x direction), is reversed at time T_E after the application of the 90° pulse. The evolution of the pulse is given as

$$m(T_E) = KA \int \rho(x) e^{j(\gamma G_x x) T_E} dx$$

$$\text{and } m(t) = KA \int \rho(x) e^{j(\gamma G_x x) T_E} \cdot e^{-j(\gamma G_x x)(t-T_E)} dx$$

$$= KA \int \rho(x) e^{j\gamma G_x x(2T_E - t)} dx$$

$$\text{for } t > T_E. \quad (3.17)$$

at $t = 2T_E$, $m(2T_E) = KA \int \rho(x) dx$,
corresponding to a rephasing.

The equations for different modalities are obtained as combination of these excitations. Appendix B lists the equations for some salient modalities and for the recovery techniques namely the SR and IR.

3.6 FID AND NMR RECEIVER :

The precessing magnetic moment $m(t)$, described by the equations (3.7) and (3.8), is picked up by a coil. The induced emf is given by Faraday's law, expressed in the form,

$$\xi = - \frac{\partial}{\partial t} (\vec{B}_1 \cdot \vec{m}(t)) \quad (3.18)$$

using the principle of reciprocity, (Hoult [22]).

\vec{B}_1 denotes the magnetic field produced by a unit current in the coil, and is assumed to be homogeneous, over the sample volume, and $\vec{m}(t)$ is the magnetic moment in the laboratory frame of reference. It is related to $m(t)$ by

$$\vec{m}(t) = m(t) e^{j\omega_0 t} \quad (3.19)$$

using the equations (3.18) and (3.19), the emf is written as

$$\xi = - j B_1 \omega_0 m(t) e^{j\omega_0 t}$$

for, the bandwidth of $m(t)$ is small compared to ω_0 (the narrow

band assumption). The coil is linearly polarized and the FID is given by

$$\begin{aligned} s(t) &= \text{Re} (-jB_1 w_0 m(t) e^{jw_0 t}) . \\ &= B_1 w_0 \text{Re}(m(t) e^{-j\pi/2} e^{jw_0 t}) . \end{aligned} \quad (3.20)$$

Figure 3.6, indicates a typical 1-D image distribution. The image is assymmetric about $x=0$, as $\rho(x)$ will in general be arbitrary, while $F(x)$ is complex. Consequently the demodulation of the FID is done at a frequency reference w different from w_0 ,

$$w \leq w_0 - \gamma (\vec{G}_r^* \cdot \vec{r}^*)_{\max} ,$$

i.e. the upper side band.

In actual NMR systems, the irradiating frequency is kept the same as the detector reference frequency w . The rotating frame analysis is then done at an angular frequency w , and the residual field along the Z-axis is given by

$$H(x) = G_x x + (w_0 - w).$$

The equations(3.6-3.8) are modified by $e^{j(w_0 - w)t}$. The magnetic moment in the laboratory frame of reference however,

is the same as in the previous analysis. This is because a change to the stationary frame is effected by a factor $e^{j\omega t}$, instead of $e^{j\omega_0 t}$.

The equation (3.20), is rewritten as

$$s(t) = A B_1 \omega_0 \operatorname{Re} \left[\left(\int_x \tilde{M}(x) e^{j\gamma G_x x t} dx \right) e^{-j\pi/2} e^{j\omega_0 t} \right] \quad (3.21)$$

where $\tilde{M}(x) = F_{xy}(x) M_0(x) L(x, t)$, is in general complex

$$\tilde{M}(x) \triangleq M_R(x) - jM_I(x) .$$

Evaluation of the real part yields

$$s(t) = A B_1 \omega_0 \left[\int M_R(x) \cos ((\omega_0 + \gamma G_x x)t - \pi/2) dx \right. \\ \left. + \int M_I(x) \sin ((\omega_0 + \gamma G_x x)t - \pi/2) dx \right]$$

Quadrature detection with reference signals $\cos \omega t$ and $\sin \omega t$, (including low pass filtering) gives,

$$s_c(t) = \frac{AB_1\omega_0}{2} \left[\int M_R(x) \cos \{ (\omega - (\omega_0 + \gamma G_x x))t + \pi/2 \} dx \right. \\ \left. - \int M_I(x) \sin \{ (\omega - (\omega_0 + \gamma G_x x))t + \pi/2 \} dx \right]$$

$$\text{and } s_s(t) = \frac{AB_1 w_0}{2} \left[\int M_R(x) \sin \left\{ (w - (w_0 + \gamma G_x x))t + \pi/2 \right\} dx \right. \\ \left. + \int M_I(x) \cos \left\{ (w - (w_0 + \gamma G_x x))t + \pi/2 \right\} dx \right].$$

Alternately,

$$s_c(t) = \frac{A B_1 w_0}{2} \operatorname{Re} \left[\int \tilde{M}(x) e^{-j\pi/2} e^{j(w_0 + \gamma G_x x - w)t} dx \right]$$

$$\text{and } s_s(t) = \frac{A B_1 w_0}{2} \operatorname{Im} \left[\int \tilde{M}(x) e^{-j\pi/2} e^{j(w_0 + \gamma G_x x - w)t} dx \right] \quad (3.22)$$

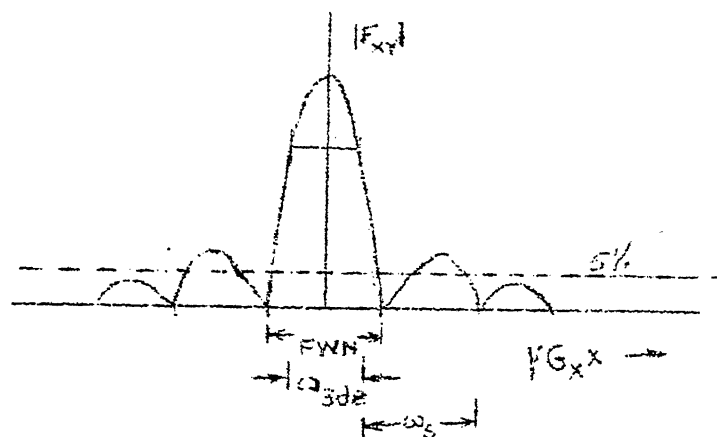
Considering that in an experiment the detector reference w is fixed, $(w_0 - w) \triangleq \gamma G_x \frac{L}{2}$, it can be seen that $\tilde{s}(t)$ ($\triangleq s_c(t) - js_s(t)$) may be Fourier transformed to obtain $\tilde{M}(x)$. The phase introduced is in general different from $\pi/2$, due to the contribution from the receiver and has to be corrected. The conceptual schematic of the receiver is shown in figure 3.5.

A special case of the equation (3.22), arises when $F(x)$ (same as $F_{xy}(x)$) = $-j$, $L(x)$ constant over x and $w = w_0$.

Here
$$s_c(t) = -\operatorname{Re} [\mathcal{F}^{-1}(M_0(x))]$$

and
$$s_s(t) = -\operatorname{Im} [\mathcal{F}^{-1}(M_0(x))].$$

This is illustrated in figure 3.6, and it corresponds to a 1-D projection of the spin image $\rho(x, y, z)$.



FWN : FULL WIDTH AT NULL

ω_{3dB} : FULL WIDTH AT HALF MAXIMA

ω_s : SIDE LOBE SPREAD

FIGURE 3.4: SELECTIVE EXCITATION

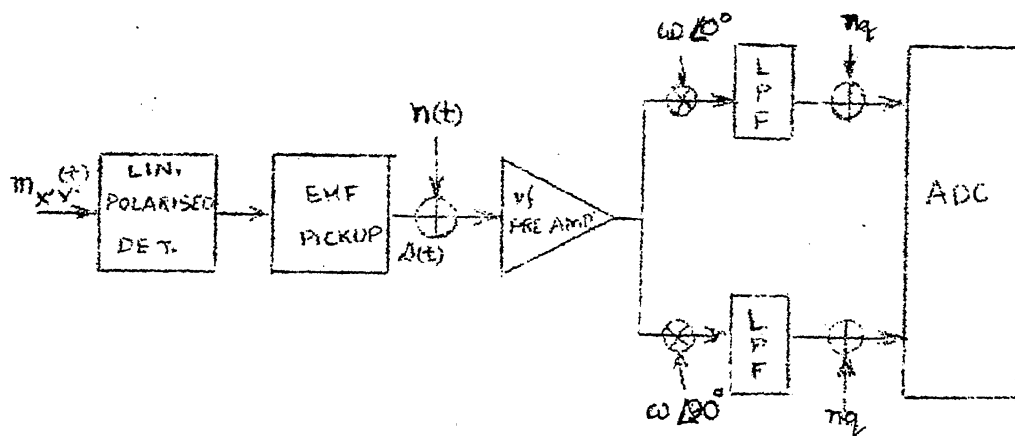


FIGURE 3.5: IMAGING RECEIVER
SCHEMATIC

$$M(x) = \mathcal{F}(\tilde{f}(t))$$

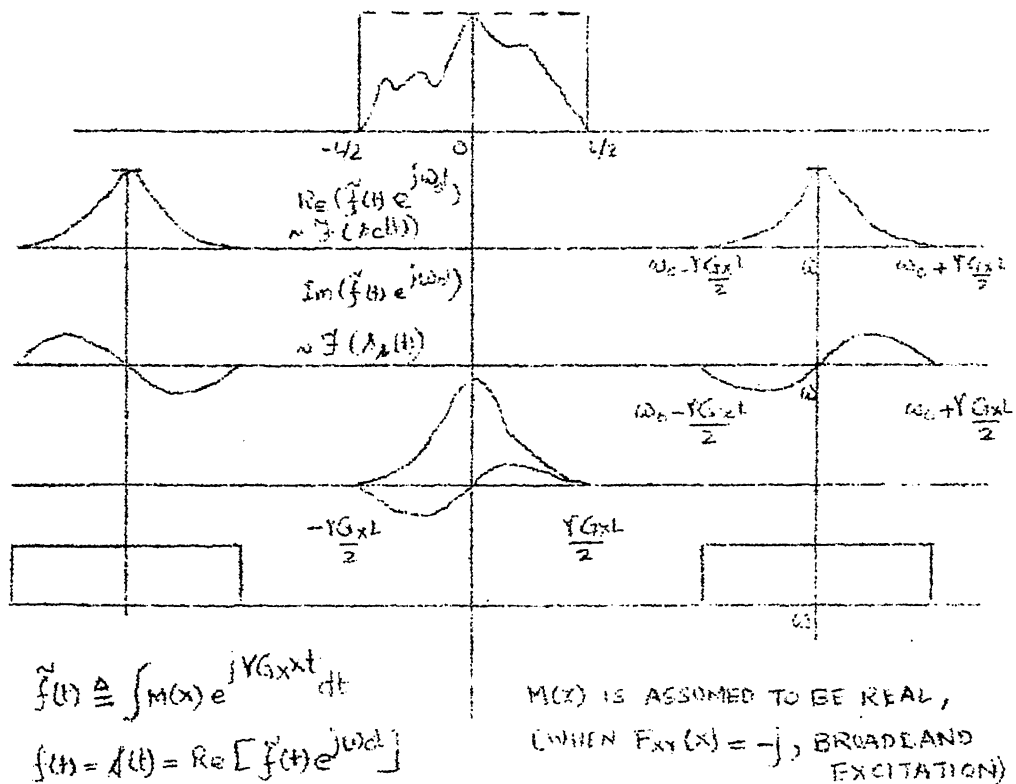


FIGURE 3.6 THE RECEIVED SIGNAL AND NOISE SPECTRUM

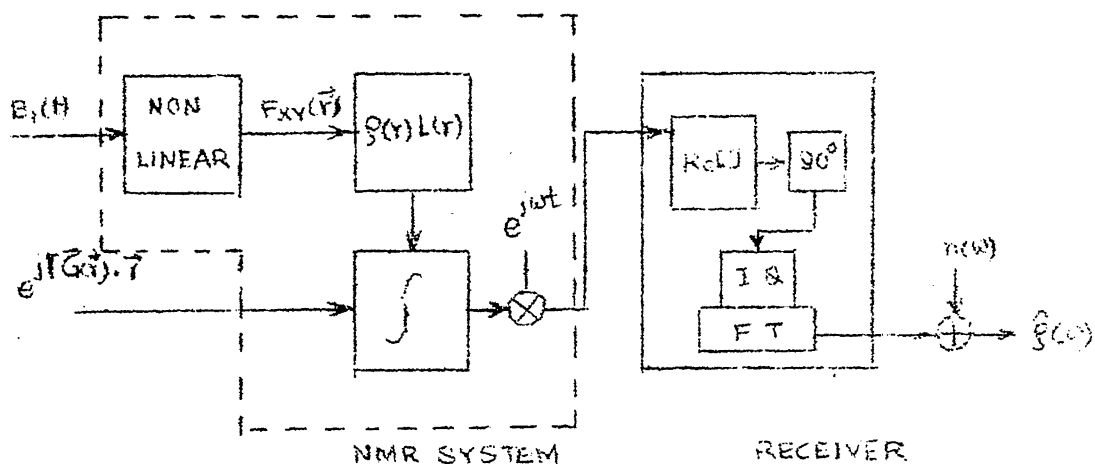


FIGURE 3.7 SYSTEM IDENTIFICATION PROBLEM

The other situation encountered is $F(x) = F_x(x) - jF_y(y)$ and $L(x)$ constant over x . This represents a selective pulse excitation, where $F_{xy}(-(x+x_1)) = -F_{xy}^*(x+x_1)$ (a conjugate skew symmetry), while $M_0(x)$ is constant over $F(x+x_1)$. x_1 is related to w (the operating frequency of the transceiver) by $w = w_0 + \gamma G_x x_1$. The quadrature component: ~~is~~ (in phase),

$$s_c(t) = \frac{A w_0 B_1}{2} \operatorname{Re} [F^{-1}(F(x))]$$

In most modalities the signal is observed in the presence of a readout gradient, describing a combination of the two cases considered above.

In addition to the FID, noise gets coupled to the system at various stages of the receiver. Its effect degrades the quality of the spin image obtained, and has to be minimized. In most NMR experiments signal to noise ratio is sufficient to determine the sensitivity, while in some imaging applications, noise statistics is warranted for developing optimum receivers, and for image enhancement.

Figure 3.6, shows the noise power spectrum along with typical a signal spectrum. The source of noise is predominantly thermal, and is assumed to be white Gaussian, around the frequency of operation. Considering the receiver

bandwidth to be larger than the signal bandwidth, the noise is assumed to be a bandpass, white Gaussian process. Denoting $n_c(t)$ and $n_s(t)$ as the quadrature noise components, $K_{sc}(\tau)$ (the cross correlation) is 0, as the spectrum of $n(t)$ is symmetric about the carrier. The two noise processes are thus, uncorrelated, and can be treated as statistically independent white Gaussian, processes with variance $N_0/2$.

The fourier transformations

$$N_c(w) = \int_{-\infty}^{\infty} n_c(t) e^{-j\omega t} dt$$

$$N_s(w) = \int_{-\infty}^{\infty} n_s(t) e^{-j\omega t} dt$$

preserves the correlation and the Gaussian property.

For a real function $M_0(w(x))$, $\mathcal{F}(s_c(t) - j s_s(t))$ is real and the reconstructed image is

$$M_0(w) = M_0(w) + N(w)$$

where $N(w) = \text{Re}(N_c(w)) + j\text{Im}(N_s(w))$

In general, where $M_0(w)$ is complex, the image may be defined as $M_0(w)$ and the noise will be a Rayleigh distributed random variable for any w .

The SNR for the experiment is evaluated, for the corresponding bandpass signal $f(t)$.

The signal is assumed to be time limited (by observation). For $M(x) = M_0$, a constant,

$$\begin{aligned}
 f(t) &= w_0 B_1 A \operatorname{Re} \left[\int_{-L/2}^{L/2} (e^{j\gamma G_x x t} dx) e^{jw_0 t} \right] \\
 &= w_0 B_1 A L \frac{\sin \gamma \frac{G_x L}{2} t}{\gamma \frac{G_x L}{2} t} \cos w_0 t \quad (3.23)
 \end{aligned}$$

The signal is gated 'on' from $t = 0$ (actually T_p , which is small compared to $1/\gamma G_x L$ and T_2).

The energy E_s in the envelope is,

$$E_s = \int_0^{\infty} w_0^2 B_1^2 V_s^2 \frac{\sin^2 \gamma \frac{G_x L}{2} t}{\left(\gamma \frac{G_x L}{2} t \right)^2} dt$$

$$= w_o^2 B_1^2 V_s^2 \pi T_2^* \quad (T_2^* \sim \frac{1}{\gamma G_x L}, \text{ for strong gradients}). \quad (3.24)$$

The maximum SNR obtainable then, is $E_s/N_o = w_o^2 B_1^2 V_s^2 \pi T_2^*/N_o$, where N_o is the white noise power spectral density (if the signal is known apriori). The ratio can then be used as a representative figure of merit, as it is based on the assumption $M(x) = M_o$. In general the spin density variations, and the T_1 , T_2 variations in the sample are small. Though the variations ($\rho(\vec{r}^>)$, $T_1(\vec{r}^>)$ and $T_2(\vec{r}^>)$) carry the imaging information (as contrast), the bulk sensitivity of the system is indicated by E_s/N_o . Additionally, this compares well with the E_s/N_o derived, for a pulsed NMR experiment, by Ernst and Anderson [11].

To sum up the system identification problem is, elaborated in figure 3.6.

CHAPTER 4

SYSTEM DESIGN CONSIDERATIONS

4.1 SYSTEM SCHEMATIC

A system identification problem was defined for NMR Imaging in the previous chapter. Figure 4.1, indicates the conceptual schematic of the system. The present chapter considers various aspects of the system, with the view of developing a design strategy. The block schematic of the system is broadly classified into five categories, in keeping with the conceptual schema. They are

1. Sample coupling
2. rf transceiver
3. Signal acquisition and averaging
4. Magnetic field control
5. Sequence control

Sample coupling, is the centre of the system, acting as an interface between the sample under study and the outside. This consists of

1. Main field coil system
2. Gradient coil system
3. The rf coil.

There are briefly described below.

1. MAIN FIELD COIL SYSTEM : This is an important part of the system, in as much as, the magnitude of the field H_0 ,

determines the operating frequency ω_0 . The spatial and temporal fluctuations over the sample, tantamounts to degradation of system performance. In high resolution NMR spectroscopy, short term temporal fluctuations, and spatial fluctuations are maintained within 1 ppm of the main field (which is typically 15-25 KG for protons and higher for other nucleides). This constraint on imaging Systems, is less stringent, due to a deliberate line broadening introduced by the field gradient. However the stability requirements on the power supply remain owing to the large sample volumes involved. Where imaging times are large, long term field drifts are traced using a known sample and frequency locking. Hoult indicates a design of an electromagnet for medium fields (~ 1.4 KG), using Helmholtz pairs on a sphere [23]. The homogeneity is reported to be 3 ppm over a sample volume of radius 10 cm.

2. GRADIENT COIL SYSTEM : Three pairs of gradient coils are used for X, Y and Z directions respectively. The first two are generated using a saddle shaped coil geometry shown in Figure 4.2. This is known to give acceptable higher order spatial field nonlinearity. The Z direction employs a Helmholtz pair, co-axial with the main field. Typical gradients acheivable in large magnets are, $\sim 0.1-0.5$ G/cm. For saddle shaped coils higher magnitudes are accompanied by greater

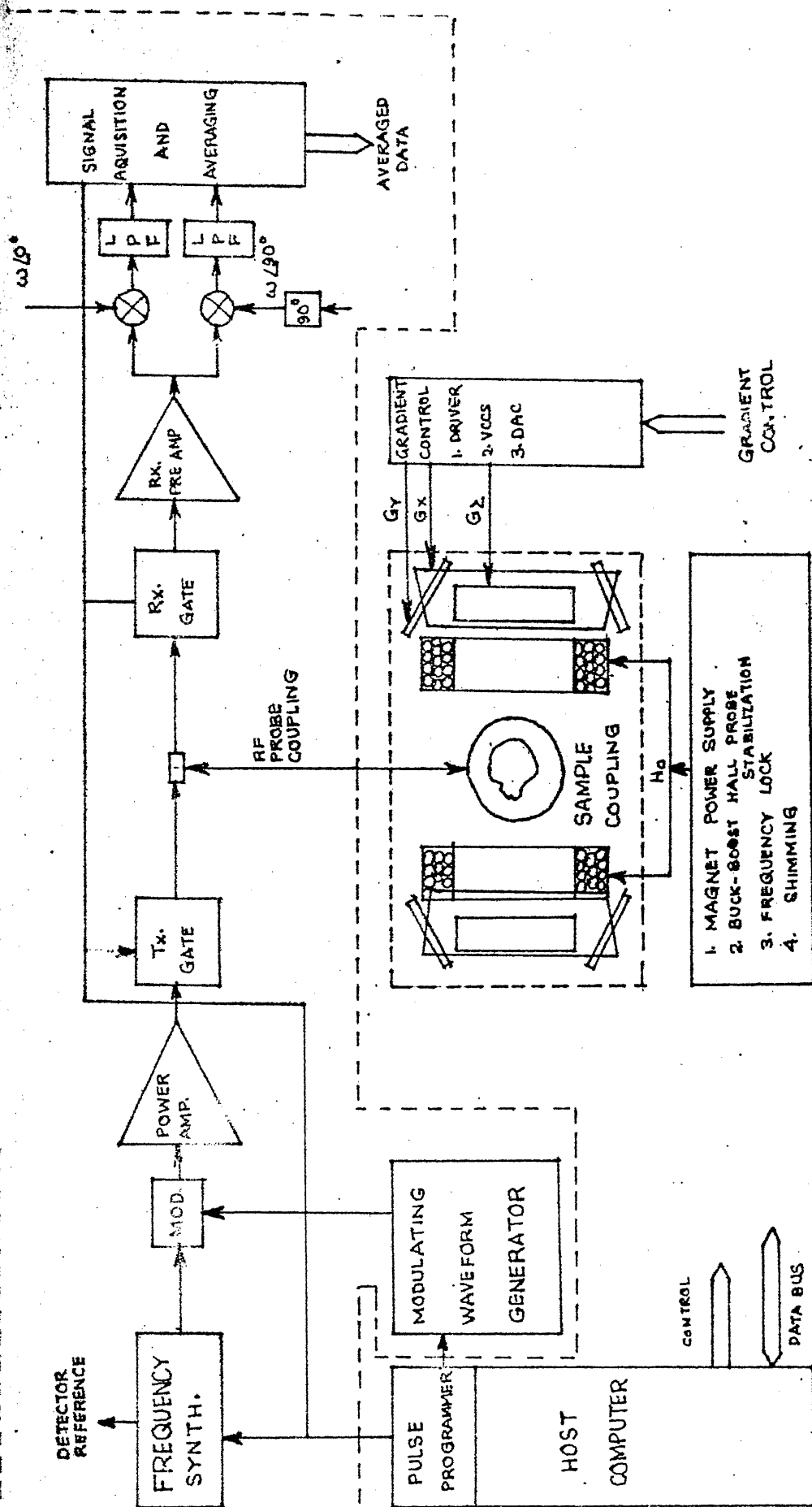
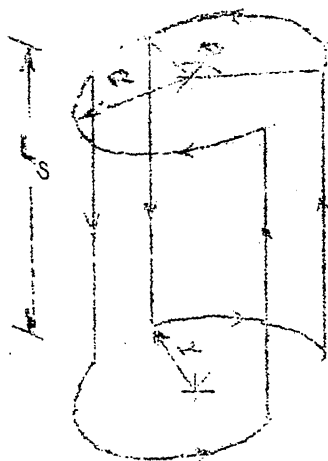
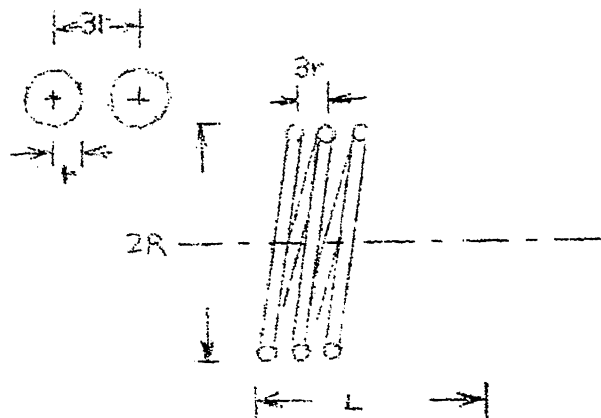


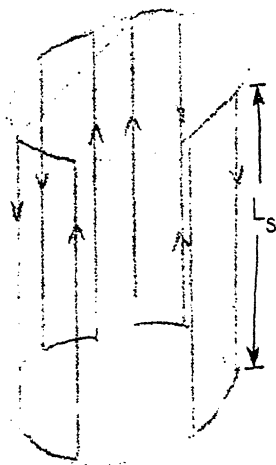
FIGURE 4.1 BLOCK SCHEMATIC OF NMR IMAGING SYSTEM



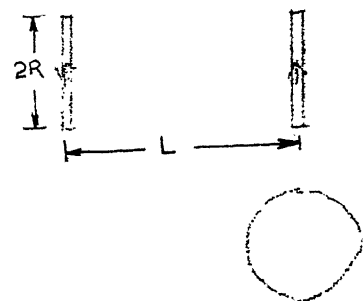
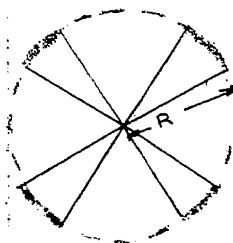
I
A SINGLE SADDLE SHAPED
PAIR



II
A SECTION OF SOLENOID



III
A SET OF FOUR COILS
FOR X AND Y GRADIENTS



IV
A HELMHOLTZ PAIR
FOR Y AND GRADIENT
(z - axis)

FIGURE 4.2 SOME COIL GEOMETRIES

nonlinearity or for a higher coil separation, higher currents. As the gradients are generally switched, the associated transients are large for high currents. Thus a compromise is sought between current, gradient magnitude, switching speed and nonlinearity. Switching times for a gradient of 0.2 G/cm (at 30A current in whole body imaging) is 1 m sec.

3. RF COIL : This couples the sample with the rf excitation. A single coil geometry is employed, usually of a solenoidal or a saddle shape , though single turn loop pairs are known to be used, in crossed coil arrangements. As these coils produce linearly polarized fields, only half the current is effective for sample excitations. The performance of the coil is measured in terms of rf field uniformity, and coupling efficiency (related to SNR). As these requirements conflict, a tradeoff is employed. For example, a solenoid has a 10dB SNR advantage over a saddle shape of same dimensions, though the field uniformity is poorer. For a radius ratio (sol. to saddle shape) ~ 2 , the SNR advantage is still ~ 7 dB, for the solenoid.

The following section presents the design considerations for the sample coupling, rf transceiver, signal acquisition and averaging subsystems, while magnetic field control and sequence control are not within the scope of this thesis.

4.2 GENERAL DESIGN CONSIDERATIONS :

The applications of NMR to clinical (e.g. proton imaging of organs) and chemical (in-vivo metabolic studies using ^{31}P) contexts are many. These areas call for different design considerations, owing to the complex interrelationship between the observables ($P(\vec{r})$, $T_1(\vec{r})$, $T_2(\vec{r})$, v) and the imaging environment. For example, detectability of lesions is more dependent on T_1 [6], while imaging of various organs are achieved by mapping $\rho(\vec{r})$ only. The modalities in these two situations are different, the former requiring methods such as inversion recovery. An overall design perspective is called for to sort out the specificities and common points, amongst different contexts.

Kaufman and Crooks [7] indicate general considerations in imaging, from the point of view of image quality, SNR and Imaging time. The choice of field strength H_0 (or the operating frequency ω_0) and modalities for achieving different goals are discussed. Wagner and Brown [24] propose the problem as an unified approach for all medical imaging methods. The detection (i.e. image acquisition from the transducer to digitization), and the display stages are distinguished. While the former determines the best possible image quality, the latter interfaces the data with a human observer. The analysis of the detection stage involves the concept of an

ideal observer, defined in the statistical sense. Image quality is related to SNR in terms of a contrast-detail curve of the form $C^2 d^n Q = \text{Constant}$, for the X-ray CT. C , d and Q denote threshold contrast, lesion diameter and SNR (or Noise Equivalent Quanta, in X-ray-context) respectively. This approach sets bounds on the detection and display stage performances.

The present discussion assumes, image quality and imaging time as 'object' parameters, for system design, along the lines of Wagner and Brown [24]. These are translated to system specifications (for the detection stage - as the discussion is on imaging hardware), namely SNR, magnetic field H_0 , Field Gradient (G_{\max}), Transmitter pulsed power W_p and the modality. Two specifications are also determined by second order effects such as,

1. Instability and Inhomogeneity of H_0 .
2. Nonlinearity of gradients
3. Non-uniformity of rf field.

over the sample. These are implementation specific and are not discussed here.

Image quality, is defined in terms of,

1. Resolution : δ_r (The smallest distinguishable section in an image).

2. Contrast : $\frac{\Delta I}{I_0}$ (normalized relative intensity of the object with respect to background)

Texture is also a parameter, and is seen to depend on the imaging hardware nonuniformities [7]. However this is not discussed here.

Resolution itself is defined in terms of,

1. A point pair
2. Contrast (in noisy images)
3. Temporal, contexts.

This parameter sets a lower bound on SNR, and is important, when signals are very weak and temporally fluctuating (as in whole body scanners and in NMR microscopy [25]). The dependence of the object criteria on the detection stage is quantified as shown in Table 4.1, while the general design considerations are summarized in Figure 4.3. This shows, that the specifications of the sample coupling, transceiver and signal processor subsystems are affected by the dimension of the sample, image quality (resolution and contrast) and imaging time. These specifications are discussed in the next section.

4.3 SYSTEM SPECIFICATIONS :

The first order design equations and the assumptions involved therein are given in Table 4.2. A comparison between the

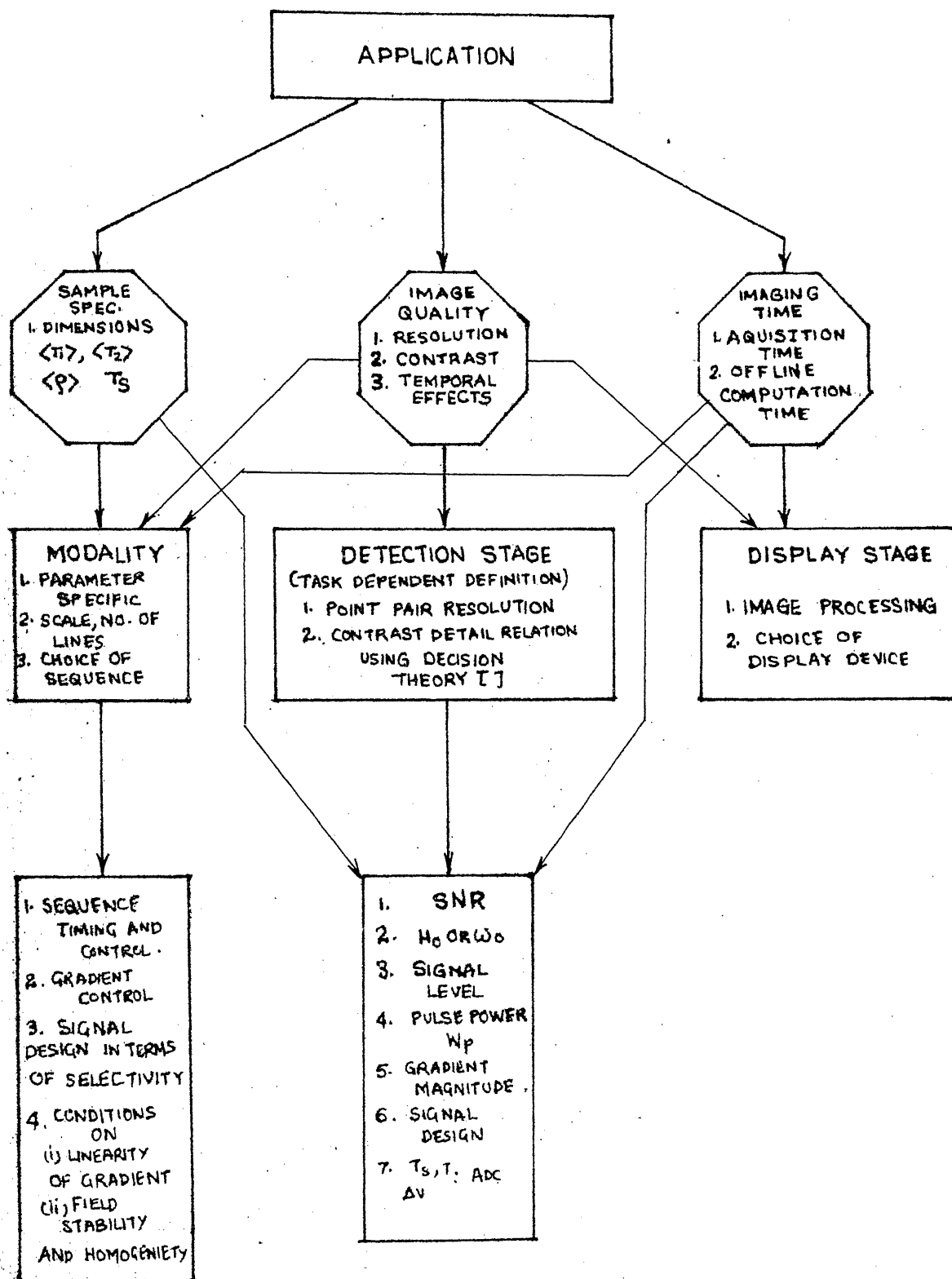


FIGURE 4.3: A SYSTEM DESIGN

two systems (a multi-phase bio-system imager and a clinical imager) is presented in Table 4.3, in the form of a case study. The response of a single 90° pulse is considered. The sensitivity of the imaging experiment is determined by the signal to noise ratio. This specification is discussed to start with.

1. SIGNAL TO NOISE RATIO :

The equation (4.1) (Table 4.2) shows the dependence of SNR on the various system variables. This is defined as a ratio of signal energy to noise spectral density, as shown in section 3.6. The SNR for an equivalent pulse resonance experiment is given by equation,

$$\text{SNR} = K_1 \cdot K_{\text{coil}} (w_0)^{7/2} \cdot \frac{T_2}{2} \cdot \frac{(\Delta V)^2}{T_\phi} \cdot G_{\text{SA}}$$

These equations are valid at frequencies, where inductive losses are not predominant. An estimate of the relative loss is quantified by the figure R_m/R_c , where R_c is the resistance of the RF coil, while R_m is the equivalent series resistance accounting for the dissipation in the lossy sample. An expression for the inductive loss is given in equations (4.4 and 4.5)* for solenoid and saddle shaped geometries respectively, Hoult [26]. Consequently the signal to noise ratio increases with a power of $7/2$ for $w_0 \ll w$ ($R_m = R_c$), (the frequency at which

* all equations are listed in Table 4.2

$R_m = R_c$), and a power of 2, for $w_o \gg w$ ($R_m = R_c$). For example, the case study (Table 4.3) indicates

$$f(R_m = R_c) = 11 \text{ MHz and } \frac{R_m}{R_c} = 3/2 \text{ at } f_o = 15 \text{ MHz}$$

$$f(R_m = R_c) = 0.89 \text{ MHz and } \frac{R_m}{R_c} = 17 \text{ at } f_o = 6 \text{ MHz}$$

respectively. These values are computed using a lossy sample, of 100 mM NaCl with a resistivity of 0.85 ohm-m. The other factors increasing SNR are the sample volume, V_s signal averaging gain G_{SA} , sample characteristics K_1 and coil factor K_{coil} . Solid or solid-like samples with lower relaxation time T_2 , have poorer SNR compared to liquid samples. A detailed discussion on G_{SA} from the point of view of modalities, is given in in Brunner and Ernst [34].

2. MAGNETIC FIELD H_o : The choice of field magnitude depends on

- a. Availability of magnets for the task,
- b. Power requirements on the magnet power supply,
- c. Complexity of electronics at the operating frequency $w_o = \gamma H_o$,
- d. The cost of performing shimming and stabilization.

These govern the economics, and technology of choice, while the advantage of increasing the field is based on the relation $SNR \propto (H_o)^{7/2}$. This is not valid for high field magnitudes and the deterring factors are

a. Self resonance effect of the coil at high frequencies. This frequency decreases with increasing coil dimensions, owing to distributed capacitances C_d . There are also associated losses in the sample dielectric proportional to C_d .

For example, in head imaging $C_d = 20$ pf, (C_d 2pf/cm diameter in solenoids), which for an inductance of $L=1\mu H$ leads to $\omega_{self} = 25$ MHz or $H_0 = 6$ KG. The dielectric losses may be represented as an effective resistance R_e , where $R_e/R = \tau Q \frac{C_d}{C}$, and τ , Q , C_d and C are loss factor, coil Q , distributed and tuning capacitances respectively (Hoult [26]). These may be minimized by reducing Q (or ω_0) or by increasing the self resonance frequency by choosing coil of smallest inductance for given dimensions with acceptable homogeneity.

b. Inductive losses in the sample are given by

$$R_m \approx K_I \frac{\pi \omega_0^2 \mu_0^2 b^5}{15 \epsilon_s}$$
, for a uniform spherical sample of radius b and resistivity ϵ_s . The expression is derived assuming negligible skin effect in the sample. For a 100mM, NaCl solution, with $b = 15$ cm, $R_m = 0.03$ ohms at 4 MHz, 0.5 ohms at 15 MHz, and 3 ohms at 40 MHz. At higher frequencies, the inductive losses are predominant, and $SNR \propto (\omega_0)^{3/2}$.

c. Radiative losses in the coil may become significant for wavelength $\lambda \sim L$ and has to be reckoned with in whole body imaging, where $L \sim 6m$, wavelength $\lambda \sim 20m$.

d. T_1 is known to increase with H_0 , implying a larger imaging time using SR and IR techniques, discussed in chapter 2.

Consequently the field cannot be increased indefinitely. Typically the operating frequency is determined by the sample losses and hardware costs. At frequencies $\omega_0 \gtrsim \omega$ ($R_m = R_c$), the SNR improvement is marginal while, the technological factors may become overwhelming. As an example, superconducting magnets for medium fields (~ 6 KG) do not give significant performance improvement. Locher [13], indicates the use of water cooled magnets at $H_0 = 1.4$ KG, for commercial applications. In Table 4.3, the fields are chosen at 3.5 KG and 1.4 KG for the two systems respectively. A value of $H_0 = 1.4$ KG is conservative, due to the small ϕ_s used. Realistic operating field range of 3-4KG is suggested for medical imaging by Kaufman and Crooks [9], by assessing the relative SNR contributions of various organs of the body.

3. FIELD GRADIENT AND RESOLUTION :

The resolution of an image increases with the field gradient as shown by the equation

$$w = \gamma (G(\vec{r}) \cdot \Delta \vec{r})$$

However increasing the gradient beyond a limit has the disadvantages that follow,

a. SNR per unit frequency decreases due to signal energy spread over a larger bandwidth, for given noise spectral density.

b. $T_2^* \sim \frac{1}{\gamma G_x L}$ decreases, rendering signal acquisition difficult, as attenuation between adjacent samples is e^{-T_s/T_2^*} . This requires signal averaging, thus increasing imaging time. This is disadvantageous, where sample movement is unavoidable.

Table 4-3, indicates a calculation for resolution. The intrinsic frequency resolution limit considered is $\Delta\nu \sim 1/T_w$, where T_w is the observation time window for the FID. In imaging experiments $T_w < T_2$. An optimistic estimate of the smallest volume observable (for a $E_s/N_o \sim 0$ dB), gives

$$V \sim 3 \times 10^{-10} \text{ m}^3.$$

$$\text{and } V \sim 7.8 \times 10^{-8} \text{ m}^2,$$

for the two systems respectively, with $T_w = 500 \mu \text{ Sec}$ or $\Delta\nu = 2 \text{ KHz}$. It may be noted that E_s/N_o is the same as the ratio of signal power in the volume to noise power in bandwidth $\Delta\nu$. This compares well with $\Delta V = 7.43 \times 10^{-10} \text{ m}^3$ by Locher [13], obtained by extrapolating SNR from the tables therein. Assuming a cube of volume $(\Delta V) = (\Delta x)^3$, the linear resolution for the two systems are

$$\Delta x \sim 0.7 \text{ mm at SNR} = 0 \text{ dB}$$

and $\Delta x \sim 4.3 \text{ mm at SNR} = 0 \text{ dB}$ respectively, while in general $\Delta x \propto \text{SNR}$. That is at $\text{SNR} = 10$, $\Delta x = 7 \text{ mm}$.

W. House [25] presents similar calculations to show resolution in microscopy context. At 600MHz, a cylindrical pill box of length $20\mu\text{m}$ and radius $2\mu\text{m}$, yields an SNR^* of 10. A frequency resolution of 1Hz is assumed for calculation.

A more realistic estimate of the resolution, has to be defined in clinical imaging context, where contrast and resolution are related, as in detection of lesions in an image field. The performance of the detection system has to be evaluated using a contrast-detail curve of the kind derived by Wagner and Brown [24]. This is also appropriate in imaging other nucleide distributions (e.g., ^{31}P), where the inherent sensitivity in terms of M_0 is poorer.

4. SIGNAL LEVEL AND TRANSMITTED POWER :

These factors are based on the dimension of the sample in as much as the coil dimensions depend on it. As such, they are dependent variables, specifying the receiver gain and power amplifier requirements. The dependence of hardware specifications on this is shown in Table 4.4. The values given in Table 4.3, are representative. They are,

Signal level :	7 μV /turn	and	0.84mV/turn
at $t=0$			
W_p :	250-100W	and	200W-1.45kW
	pulsed rms		pulsed rms
	for T_p 5-10		for T_p 500-100
	$\mu\text{Sec.}^p$		$\mu\text{Sec.}^p$

* POWER SNR ($\approx 10\text{dB}$)

for the two systems respectively. As the number of turns in the coil (n) is specified by the coupling circuit configuration, the emf induced is expressed in volts per turn. The transmitted power (pulsed rms value) is derived by assuming that the power coupled to the rf circuit is dissipated wholly in the sample coil and the sample itself. Equation (4.6) indicates a $1/T_p^2$ dependence between pulse duration T_p and W_p , and a ϕ^2 dependence between the flip angle and W_p . Consequently, it is unrealistic to produce broadband 180° pulses in high gradient experiments. Spin echo is usually effected by the use of gradient reversal (which again is speed limited due to switching rise time). For example, W_p for a 180° , 50 μ Sec rectangular pulse is 6 kW, while for a 25 μ Sec pulse would be 24 kW. However, as 180° pulses are used to produce spin echo, its duration may be greater than 50 μ Sec. The power requirement continues to be large, considering dissipation in other parts of the transmitter circuit.

5. SIGNAL ACQUISITION AND SAMPLING :

The FID after demodulation is recorded digitally. The minimum sampling rate F_s required is determined by the Nyquist criterion, $F_s > 2$ (B.W. of the signal), while the number of samples per unit bandwidth is determined by resolution considerations. The intrinsic resolution is assumed to be $1/T_w$, where T_w is the acquisition window. The FID is, $V_s = V_0 e^{-t/T_2^*}$

(actually it is more realistic to approximate as

$V_s = V_0 \text{ sinc} \left(\frac{\gamma G_x L t}{2} \right)$ and $T_2^* = \frac{1}{\gamma G_x L}$). This corresponds to the signal for a 1-D projection for a gradient in one direction.

Calculation of the time T at which $V_s \sim \langle n^2 \rangle^{1/2}$ (the rms noise voltage), yields a lower limit on the observation time. Table 4.3, indicates a sampling rate, sampling interval and the acquisition time $T(V_s = \langle n^2 \rangle^{1/2})$ of 70 KHz, 15 μ Sec and 600 μ Sec for a 50 μ Sec decay signal and 400 KHz, 2.5 μ Sec and 100 μ Sec for the two systems respectively. The contribution of the receiver noise is not accounted for and hence this gives an optimistic estimate.

This indicates a total of 40 samples in the observation duration for both cases. In reality the number of samples acquired in a single experiment is more, i.e., the observation time may be more than T , defined above. This is because, though the signal level goes below the noise level $\langle n^2 \rangle^{1/2}$, the total SNR of the experiment (or SNR over the frequency spectrum) is within acceptable limits. The evaluation is shown in the preceding section.

Consequently the acquisition time T_w , is limited by rf pulse repetition rate (or modality e.g., IR and SR sequences).

Typically for $T_2 = 50\text{mSec}$, T_w may be as large as 25mSec , as shown by Locher [13]. The minimum number of samples required is determined by the ratio, $K = \gamma G_x L / 2\pi \Delta \nu$ or $K = L / \Delta x$ (where $\Delta \nu = 1/T_w$, the resolution limit in frequency and L the length of the sample). For the two systems under study K (maximum required for a resolution at $\text{SNR} = 0\text{dB}$) is 30 and 60 respectively. More number of samples or pixels in an image for a given T_w , does not improve this resolution, though may be convenient for viewing and interpretation.

4.4 AN IMAGING SYSTEM FOR MULTIPHASE BIO-SAMPLES

The first order calculation, based on the expressions given in Table 2, are performed for an imaging system used in multiphase bio-sample study. The results of the calculations are summarized in the first column of Table 4.3. The assumptions involved are listed below :

1. The imaging requirement given in the beginning of Table 4.3, cover major bio-samples of interest.
2. A spherical sample of resistivity $\rho_s = 0.15 \text{ ohm-m}$ (100mM NaCl solution (Hoult [26])) is used for evaluating inductive losses. This yields a value of R_m on the conservative side.
3. The effective volume of the coil ($\sim 5 \times 10^{-5} \text{ m}^3$) is ten times the total sample volume, ensuring good homogeneity in

the saddle shaped (Bernardo [29]) and solenoid coils .

4. The iron magnet available, generates a 15KG field, at a current $\sim 30-40A$, while the saturation current is less than 50A.

5. Imaging time is not a premium, as the sample movement is restricted.

The design values calculated namely,

$$H_0 = 3.5 \text{ KG}$$

$$V_s(t=0^+) = 7\mu V/\text{turn}$$

$$W_p(180^\circ) = 300W \text{ (dissipation in the coil and sample only)}$$

$$W_{avg} \sim 10W$$

and $T_s \sim 15\mu\text{Sec.}$

are implementable with existing pulsed NMR facilities

The gradient required for 1mm resolution (corresponding to

$\Delta\nu \sim 2\text{KHz}$) is $\sim 5G/\text{cm}$ while with a 200 Hz resolution is 0.5 G/cm. The band spreading due to a gradient of 0.5G/cm over 5 cm of sample is 10KHz or the decay time constant is 20 μSec (for an equivalent exponential). The limiting factor on resolution is then the signal to noise ratio. The previous section indicates an SNR of 0dB at 1 mm resolution. The performance may be improved by signal averaging at the cost of imaging time. Repeating the experiment ten times gives an

SNR of 10dB at 1 mm resolution. The ampere turns required for the gradient (0.5G/cm) is 12AT for a Helmholtz pair of $R/L=1$ and 19AT for $R/L=1/2$.^{*} The ratio $2R/L=1$ is optimum in the sense that, the second and third derivatives at the centre of the coil are equal to zero.

The signal to noise ratio, $E_s/N_o = 70\text{dB}$ for $T_2^* = 2.27 \times 10^{-4}$ Sec and 55dB for $T_2=50\mu\text{Sec}$, for the whole sample excitations. This corresponds to the FID from a single image projection. A set of six projection in a plane are tractable for reconstruction of the image, considering the software complexity. The resulting E_s/N_o is 77dB (taking into account signal averaging). The corresponding (0dB SNR) resolution is $\Delta V = 5.32 \times 10^{-10} \text{ m}^3$ (or $\Delta x = 1\text{mm}$). In practice $\text{SNR} < E_s/N_o$, as noise and signal bandwidths are not matched. This may correspond to an SNR degradation of upto 10dB (after accounting for receiver noise). (Considering the complexity of selective excitation and gradient switching, projection reconstruction is a plausible modality for the application).

* FIGURE 4.2, p-74.

TABLE 4.1
IMAGE QUALITY AND SYSTEM PARAMETERS

RESOLUTION		CONTRAST	IMAGING TIME
SPATIAL RESOLUTION	TEMPORAL RESOLUTION		
Gradient T_2	1. Sample motion e.g. random fluctuations in sample	$\rho(r)$ T_1 T_2	Modality Signal Avg. required(+)
FWHM OF F_{xy}	2. Drift in detection System	v	Computational power (-)
SNR in Noise Limited case		Contrast inducing agents	Sample movement (-)

TABLE 4.2

FIRST ORDER DESIGN EQUATIONS

EQUATION	REF.	ASSUMPTION
SNR :		a. B_1 is constant over the sample volume
$N_o = K_1 \cdot K_{coil} \cdot (w_o)^{7/2} \pi T_2^*$ $\frac{(\Delta V)^2}{T_c} G_{SA} \quad (4.1)$	Hoult [26],	b. Self resonance, radiative losses in the coil neglected.
working equation, $N_o = \frac{w_o^2 M_o^2 (\Delta V)^2 \pi T_2^*}{4K T_c} \cdot \frac{B_1^2}{R}$ (4.2)	Ernst [11]	c. Effect of finite T_R (the repetition interval is neglected)
re		
$= R_c$ (sample losses neglected)		
$= R_c + R_m$ (inductive losses present)		
general		
$\frac{1}{R} \sim \frac{B_1^2}{(\alpha w_o^{1/2} + \beta w_o^2)}$ $\alpha w_o^{1/2} \ll \beta w_o^2 \Rightarrow \text{negligible losses}$ $\beta w_o^2 \gg \alpha w_o^{1/2} \Rightarrow \text{losses predominant}$		
SAMPLE LOSSES	Hoult [26].	a. All dielectric loss effects are lumped into τ
electric $R_e = \tau Q \frac{c_d}{c} R$		b. Electric field due to C_d only
active $R_m = \frac{K_I w_o^2 \mu_o^2 b^5}{P_s}$		c. Sample modelled as a sphere of radius (b) and uniform resistivity (P_s) .
skin effect $\delta_s = \sqrt{\frac{2 P_s}{\mu_s \mu_o w_o}}$		d. skin effect neglected
	(4.3)	e. Losses are lumped to an equivalent resistance R_e or R_m .

• COIL FIGURE OF MERIT

$$\sim B_1^2 / R_c$$

• COIL GEOMETRIES

a. Solenoid :

$$|\vec{B}_1|_0 = \frac{n\mu_0}{2} \frac{1}{(R^2 + (L_s/2)^2)^{1/2}} \quad n \gg 1$$

Hoult
[26]

$$R_c = \frac{3\sigma\varphi n^2 R}{8 L_s}$$

Henney
[27]

$$\delta = \sqrt{\frac{2\varphi}{\mu\mu_0 w_0}}$$

$$L = n^2 R^2 \left[\frac{0.0395}{1 + 0.9(R/L_s)} \right] \mu H$$

R and L_s are in cm.

$$B_1^2 / R_c = \frac{\mu_0^2 \delta}{12\sigma\varphi R^2}$$

for $\frac{L_s}{2R} \approx 1$ and coil separation $3r$.

$$R_m = \frac{n^2 \pi w_0^2 \mu_0^2 b^5}{30 \varphi_s (R^2 + (L_s/2)^2)} \quad n \gg 1 \quad (4.4)$$

• Saddle Shaped

$$|\vec{B}_1|_0 = \frac{4\mu_0 n (\frac{L_s}{2}) (\frac{1}{s^2} + \frac{3}{2}) \sin \frac{\varphi}{2}}{\pi R^2} \quad \text{Ginzberg [28]}$$

$$s \triangleq 1 + (\frac{L_s}{2R})^2$$

$$R_c = \frac{\sigma n \varphi (4\varphi R + 4L_s)}{2\pi \delta r} = \frac{60 n^2 \varphi \sigma}{\pi \delta} (\frac{\pi}{3} + 1)$$

$$L = (2R_L) |\vec{B}_1|_0$$

$$\frac{B_1^2}{R_c} = \frac{\mu_0^2 \delta}{20\pi} \cdot \frac{1}{\sigma \varphi R^2} \times \frac{(-\frac{1}{2} + \frac{3}{2})^2}{(\frac{\pi}{3} + 1)}$$

for $\frac{L_s}{2R} \approx 1, (n-1)3r < \frac{L_s}{10}$

(4.5)

and $\varphi = 120^\circ$

1. n_0 the number of turns is large for a solenoid.
2. σ is a proximity factor, relating to neighbouring field effects
3. distributed effects (c_d) are not considered
4. $\mu_r = 1$
5. The width of the saddle section, $(n-1)3r < L/10$

EQUATION	REF	ASSUMPTIONS
. TRANSMITTER POWER REQUIREMENTS		
$W_p = \left(\frac{2\pi}{\gamma T_p} \right)^2 \left(\frac{R_c}{B_1^2} \right) \cdot \frac{1}{2}$	Hoult [22]	1. All power is dissipated into the coil resistance
for a 180° pulse		2. Only half the current in the coil goes towards generating the rotating field.
and $W_{avg} = W_p \frac{T_p}{T_R} \quad (4.6)$		
. PULSE DERINGING TIME		
important in single coil rf probes)		
$\tau_d = \frac{2Q}{\omega_0} \quad (4.7)$		-
. PULSE DURATION		
roadband $T_p = \frac{1}{\gamma G_x L} \quad (4.8)$		a. $\gamma G_x L \gg 1/T_2$
narrowband rectangular pulse :		-
$\text{inc}(\gamma(B_1^2 + (G_x \Delta x)^2)^{1/2}) T_p = \frac{1}{\sqrt{2} \pi} \quad (4.9)$		-
. INDUCED emf		
$s(t) \Big _{t=0} = \omega_0 B_1 M_0 \Delta V \quad (4.10)$		-
. GRADIENT		
$\Delta f = 4257.6 G_x \text{ Hz/cm}$		
$\delta f = \Delta f \delta x G_x \text{ Hz}$		a. An approximation for the SNR.
$\frac{(s_0)^2}{N_0} = \frac{\omega_0^2 \mu_0^2 T_w B_1^2}{4KT_c R} \left(\frac{1}{R} \right) (\Delta V)^2$		
for resolution : $(\delta x)^3 = (\Delta V)$		b. Obtained by using the Biot-Savart law and evaluating $\partial \delta / \partial Z \Big _{Z=0}$
$I_0 = \frac{\mu_0 I (2\pi R)}{4\pi R^2} \quad (K)$		
$2\pi L = R$ Saddle shaped coil		
$\sim 10 L = 2R$ Helmholtz pair		
(4.11)		

Legend for the table 4.2 :

K_1	sample characteristics
K_{coil}	coil characteristics
ω_0	operating frequency (ωH_0)
T_2^*	signal decay time
ΔV	sample volume
T_c	coil temperature
R_c	coil resistance
R_m	resistance for sample induction loss
R_e	resistance for sample dielectric loss
b	sample radius
ρ_s	sample resistivity
δ_s	sample skin depth
B_1	field due to unit current in the coil
ρ_c	coil resistivity
L_s	length of the coil
R	coil radius
δ	skin depth in copper
ϕ_s	angle subtended by saddle at the axis of the coil
n	number of turns in the coil
r	radius of the wire
τ	dielectric loss factor
Q	coil quality factor
c_d	coil distributed capacitance
c	tuning capacitance
T_p	pulse duration
T_R	pulse repetition interval
τ_d	deringing time
Δx	object element size
T_w	observation window
I_0	current required in the gradient coils
K	geometric factor for the gradient coils

TABLE 4.3

CASE STUDY

$$\begin{aligned}
 T_s &= 310^\circ\text{K} & \gamma/2\pi &= 42.576 \text{ MHz/Tesla.} \\
 T_c &= 310^\circ\text{K} \\
 M_o &= 3.25 \times 10^{-3} \text{ H}_o \text{ A m}^{-1} \text{ (for protons in water)} \\
 \rho_c &= 1.69 \times 10^{-8} \text{ ohms. m} \\
 \rho_s &= 0.85 \text{ ohms m (100mM)} \\
 &\text{NaCl (Saline solution)}
 \end{aligned}$$

Proton Imaging

SYSTEM SPECIFICATION	IMAGING SYSTEM FOR MULTI-PHASE BIO-SAMPLES	CLINICAL IMAGING SYSTEM
T_1	50-500m sec	50-500m sec
T_2	50μsec-500μsec (or higher)	500μsec-50msec [13]
Sample size	1cmx3cmx1cm	20cmx20cmx25cm
Total sample volume V_s	$3 \times 10^{-6} \text{ m}^3$	0.01 m^3
Typical object contrast $\langle \Delta \rho(r) \rangle / \langle \rho(r) \rangle$	2-5%	2-5%
T_1, T_2 variations	10%	10%
Resolution required	~ 5mm	~ 5mm
Magnet available	Iron Magnet (gap): $5\text{cm} \times (\pi(\frac{15}{2})^2 \text{ cm}^2)$ Saturation current ~ 50A	$V_c = 0.02 \text{ m}^3$ For a saddle shaped coil $V_s = 2V_c$, gives uniform field within 20% over the sample [29]
RF Probe	Solenoid: $R=2\text{cm}$ $L=4\text{cm}$ Saddle shape: $R=2\text{cm}$ $L=4\text{cm}$ $\phi=120^\circ$	saddle shaped: $R=15\text{cm}$ $L=30\text{cm}$ $\phi=120^\circ$

continued

SYSTEM SPECIFICATION	IMAGING SYSTEM FOR MULTI-PHASE BIO-SAMPLES	CLINICAL IMAGING SYSTEM	
Linear Gradient achievable (Typical)	0.05-1.0G/cm within 10% linearity	0.1-0.2G/cm within 10% linearity	
Choice of field H_0	$f_0(R_m=R_c)=11\text{MHz}(\text{Sol.})$ $f_0(R_m=R_c)=50\text{MHz}(\text{Saddle})$ at $f_0 = 15\text{MHz}$ $(\frac{R_m}{R_c})_{\text{sol}} = 1.5$	0.899MHz at $f_0=15\text{MHz}$ 17.21	
	$(\frac{R_m}{R_c})_{\text{saddle}} = 10.16$ $w_{\text{self}} \leq 50\text{MHz}$ $\delta_g = 12 \text{ cm}$ $I(15\text{MHz}, 0.35 \text{ Tesla}) \sim 35\text{A}$ $H_0 = 0.35 \text{ Tesla}$	$\leq 20 \text{ MHz}$ 19cm - $H_0=0.14 \text{ Tesla}$ In medical imaging [9], optimum field is 3-4KG, due to lower φ_g .	
SNR	Sol.	Saddle	
B_1^2/R_c	1.096×10^{-7}	1.151×10^{-8}	3.24×10^{-10}
B_1^2/R_T	4.39×10^{-8}	9.9×10^{-9}	1.9×10^{-11}
E_g/N_0	73.2dB	67.7dB	19dB
	(for $T_2^*=2.27 \times 10^{-4}\text{sec}$)	(for $T_2=500\mu\text{sec}$)	
	58.6dB	52.22dB	80dB
$\Delta V=1 \times 10^{-6}\text{m}^3$	(for $T_2=50\mu\text{sec}$)	(for $T_2^* = 6.3\mu\text{sec}, V=0.01\text{m}^3$)	
Signal level (at $t=0$)	7.150nV at $\Delta V = 3 \times 10^{-6}\text{m}^3$	11.8nV	0.84n. mV

continued

SYSTEM SPECIFICATION	IMAGING SYSTEM FOR MULTI-PHASE BIO-SAMPLES	CLINICAL IMAGING SYSTEM
----------------------	--	-------------------------

Resolution

$$\frac{s^2}{N_0 \cdot (1/T_W)} = 0 \text{ dB}$$

$$T_W = 500 \mu\text{sec} \quad 2.6 \times 10^{-10} \text{ m}^3 \quad 5.5 \times 10^{-10} \text{ m}^3 \quad 7.82 \times 10^{-8} \text{ m}^3$$

$$T_W = 50 \text{ msec} \quad 2.6 \times 10^{-11} \text{ m}^3 \quad 5.5 \times 10^{-11} \text{ m}^3 \quad 7.82 \times 10^{-9} \text{ m}^3$$

$s^2/N_0(1/T_W)$ is a first order approximation,
and typically $\frac{E_s}{N_0} \left(\frac{E_s/T_W}{N_0/T_W} \right)$, the SNR may be used.

$$R_T \quad 0.011 \text{ n}^2 \text{ ohms} \quad 0.117 \text{ n}^2 \text{ ohms} \quad 1.26 \text{ n}^2 \text{ ohms}$$

$$\langle n^2 \rangle^{1/2} \quad 6.94 \text{ nV}/\sqrt{\text{Hz}} \quad 22.4 \text{ nV}/\sqrt{\text{Hz}} \quad 74 \text{ pV}/\sqrt{\text{Hz}}$$

Pulsed Power Requirements (W_p)

Broadband	<100W pulsed rms ($T_p = 10 \mu\text{sec}$, $\phi = 180^\circ$)	<100W ($T_p = 500 \mu\text{sec}$, $\phi = 180^\circ$) ~6KW ($T_p = 50 \mu\text{sec}$, $\phi = 90^\circ$) ~25W ($T_p = 500 \mu\text{sec}$, $\phi = 90^\circ$) ~1KW ($T_p = 50 \mu\text{sec}$, $\phi = 90^\circ$)
Without Gradient	250W ($T_p = 5 \mu\text{sec}$, $\phi = 180^\circ$)	~1.45-6KW ($T_p = 100-50 \mu\text{sec}$, $\phi = 180^\circ$) ~350W-1.45KW ($T_p = 100-50 \mu\text{sec}$, $\phi = 90^\circ$)
W_{avg}	6.5-10W for $T_R \sim 200 \mu\text{sec}$	0.4-10W for $T_p/T_R \sim 10^{-3}$

SYSTEM SPECIFICATION	IMAGING SYSTEM FOR MULTI-PHASE BIO-SAMPLES	CLINICAL IMAGING SYSTEM
<hr/>		
Signal aquisition time		
$\frac{\gamma}{2\pi} G_x L$	$\sim 700-3500 \text{ Hz}$	$12.7 - 25 \text{ KHz}$
T_2^*	$\sim 2 \times 10^{-1}$	$1.25 - 0.63 \times 10^{-5} \text{ sec}$
Sampling rate F_s	$\geq 2 \times 10 \times \frac{1}{2\pi T_2}$ $= 70 \text{ KHz}$ $(T_2 = 50 \mu\text{sec})$	$\geq 2 \times \frac{1}{T_2} = 400 \text{ KHz}$
Sampling interval T_s	$\sim 15 \mu\text{sec}$	$2.5 \mu\text{sec}$
Aquisition time T_a (without averaging)	$6.57 \times 10^{-4} \text{ sec}$ (for $V_0 / \langle n^2 \rangle^{1/2} = 1$)	$100 \mu\text{sec}$
Maximum number of samples	~ 40	~ 40

HARDWARE AND SYSTEM SPECIFICATION

SUBSYSTEMS	SPECIFICATIONS	TYPICAL VALUES	DEPENDENCE
Sample coupling Magnetic Field H_0	Field Strength Order of current Req'd.	3.0-4.0 KG ~ 30A	Determined by optimum field considerations For pole separation 3" and Area: $\pi(6")^2$ (i.e. by scale of the experim
	Homogeneity	1 in 10 ²	
	Stability	1 in 10 ⁵	
Gradient G max	Magnitude (max.)	~ 0.1 G/cm	Resolution, SNR and Imaging Ti
	Order of current	~ 1 A max.	For same pole gap Given above
	Switching speed, Rise Time	100nsec. - 1msec	Gradient magnitude, Apollicati
	Frequency		Readout, Switching, Transients
			Pulse or reversal-Imaging Tim
RF Coil	Geometry	Solenoid for Small, saddle shaped large samples	B_1^2 R_c Homogeneity v/s
	Coil Temperature (cooling etc)	300°K (water -cooled)	SNR advantage v/s hardware complexity
Receiver	Preamplifier Gain	-	Signal Level: T_2^*
	Noise Figure/Temperature	4DB	Determined by (SNR) coil
	Bandwidth	MHz	Determined by T_2^*
Transmitter	Transmitter W_p , W_{avg}	1KW, 10W max	Determined by dimension of sam ple and nature of excitations
	Bandwidth	-	Maximum $1/T_2^*$, Rise Time
	Gain	-	Determined by input signal lev
Others (Implementa- tion dependent)	RF switch isolation	~ 60 dB in pulsed NMR	W_p receiver protection
	Saturation recovery of receiver TR	-	Amplifier gain
	Mixer insertion loss	-	Depends on choice of Mixer, Biasing Circuits and cost
	Coil inductance	1-120uH for 15MHz-3.5KG effects	Circuit, SNR, self resonance
	Coil Q	~ 100	Neglecting C_d
	Low pass filter specification	-	By band width and T_2^* , Preferat be a minimum delay filter.
Data Aquisition S/H specifications	Acquisition time Hold Error Conversion Time		Determined by over sampling re ADC speed requirements, usual
	Resolution		Flash Conversion employed Computational accuracy image

CHAPTER 5

A PULSED ~~rf~~ TRANSCEIVER

5.1 TRANSRECEIVER REQUIREMENTS :

The specifications for the design of the rf-coupling ^{are considered here} the transmitter and the receiver. The NMR imaging applications are discussed in chapter 4. Tables 4.3 and 4.4 present a case study of an NMR imager for multiphase bio-specimen, and the parameters to be specified on the transceiver. The present chapter discusses the design of an rf coupling circuit and transceiver configurations for the application.

The basic constituents on the rf transmitter-receiver are listed below :

Transmitter :-

1. Impedance matching with load (the sample coil resonant circuit),
2. High pulsed power from the transmitter amplifier,
3. Small post-transmit pulse ~~dering~~ ringing time τ_d ,
4. Short power amplifier rise time (or large bandwidth),
5. Modulating signal design for selective pulse excitations
6. Transmit switch offering low 'on' attenuation and high 'off' isolation, to decouple transmitter noise from the sample coil during reception of FID.

Receiver :-

1. Low Noise Figure for the preamplifier,
2. Efficient noise, and signal power matching of the source (the sample coil) with the receiver preamplifier,
3. Quadrature demodulator for the recovery of the base band signal (with anti-aliasing filter),
4. rf switches with high isolation to protect the receiver from high power rf pulses and low 'on' attenuation, and shot noise contribution, during signal reception.

The similarity with the Radar Context may be noted.

Figure 5.4 illustrates a typical excitation - reception sequence in imaging, with the various timings involved therein. The Table 5.1, lists the specifications for the system under development. The deringing time τ_d is estimated for the worst case values of T_2^* and T_2 . The resistance (R), inductance (L), quality factor (Q_c max.) and the distributed capacitance C_d of the coil are given along with peak and average current (I_p and I_{avg}) and the rf field (B_1) requirements for $T_p \sim 5\mu\text{Sec}$ and $\phi = \pi/2$.

The specifications for the ENI-series broadband power amplifiers and the Matec series rf preamplifiers are assumed in the design of the coupling circuit given in the following section.

5.2 rf COUPLING CIRCUIT

The design is based on the following observations :

1. The pickup coil (same as the transmitter coil, for single coil probes) is an inductive source (or load) with an inductance given by $L=Cn^2$, where C is a constant determined by the geometry and the dimension of the coil, and n is the number of turns in the coil. Here n is a variable, within physically realizable limits,
2. The received signal and the excitations are narrow band, so that tuned circuits may be employed.
3. The excitation rf field B_1 is proportional to the current in the coil, which is maximum in series resonance circuits for a given external driving voltage.

Consequently, the circuit design for series resonant circuit is considered in this thesis. A starting point is the circuit shown in Figure 5.1, due to Clark and McNeill [30]. Three sets of independently tuned circuits are employed as shown. C_I and C_{II} are chosen to meet the transmitter requirements while C_{III} is obtained from noise matching considerations. The switches S_1 and S_2 are the transmitter-receiver switches, closed during excitation and open during reception. The transmitter coupling design is obtained by

maximizing the field with the sample coil L_2 , within the constraint of τ_d . An assumption, that only half the energy in the coil is stored within its confines, is made to relate B_1 with I_T (Figure 5.1). This is not valid for saddle shaped coils, where the field concentration is near the conductors.

The results of the calculations are indicated in Table 5.2. The choice of L_2 is made based on minimum number of turns required on a solenoid for nominal field homogeneity within the coil. The field achieved is $B_1 \sim 0.75 B_{1 \text{ max}}$, where $B_{1 \text{ max}}$ is the maximum field for a given current I_T . The design indicates large power dissipation ($\sim 3\text{ kW}$ pulsed rms) in the external resistor $R_g = 21 \text{ ohms}$, employed to reduce Q_T . The impedance match, $Z_L = 38.5 - j27.9 \text{ ohms}$, is also poor. As such this transmitter coupling circuit configuration is not well suited for imaging where power requirements are large.

The receiver coupling configuration R_3, L_3, C_3 is optimum for noise matching of narrow band resistive signal sources with the preamplifier (Yishay Netzer [31]). The design is carried out assuming an $\bar{e}_n^>$ (equivalent input series noise voltage source) and $\bar{i}_n^>$ (the equivalent input shunt noise current source). The SNR, optimum ratio (L_3/C_3 for minimum SNR) and the matched noise figure (NF) are expressed, as :

$$\text{SNR} = \frac{e_s^2}{4kTR_s + R_s^2 \overline{i_n^2} (1 + L/R_s^2 C) + \overline{e_n^2} R_s^2 C/L}$$

$$(L_s/C_3)_{\text{opt}} = R_s \sqrt{\overline{e_n^2}/\overline{i_n^2}} = R_s \frac{\overline{e_n}}{\overline{i_n}}, (L_3 C_3)^{-1/2} = \omega_0$$

$$(\text{NF})_{\text{matched}} = 10 \log_{10} \left(1 + \frac{\overline{e_n} \cdot \overline{i_n}}{2kT} \right).$$

For typical FET input stages, $\overline{e_n} \sim 10\text{-}25\text{ nV}/\sqrt{\text{Hz}}$ and $\overline{i_n} \sim 1\text{ pA}/\sqrt{\text{Hz}}$. This yields a noise figure of $\sim 6\text{ dB}$, $(L_3/C_3) \sim 25500$, while L_3 and C_3 are $1.7\text{ }\mu\text{H}$ and $60\text{-}70\text{ pf}$ respectively. As such given preamplifier, a knowledge of $\overline{e_n}$ and $\overline{i_n}$ are required to obtain noise matching. The Matec 615 tuned receiver available guarantees 6 dB noise figure at 50 ohms input impedance. The variation of the NF around the optimum ratio is small for low noise amplifiers (Netzer [31]). As a result small mismatches do not affect the noise performance of the amplifier.

An alternative coupling circuits is shown in figure 5.2. The impedance matching is obtained by the capacitor C_m while Q control is effected through the use of a resistor $R_s \sim 10\text{ ohms}$.

The residual reactance $X_r = 1/\omega C_m$, may be tuned out with the inductance L_m , through impedance matching. The series circuit R_2, L_2, C_2 is detuned by a factor $\Delta = \omega L_2 - \frac{1}{\omega C_2}$, to obtain matching with C_m . To keep the residual reactance $\frac{1}{\omega C_m}$ at 10 ohms Δ must be equal to 5. Consequently for receiver tuning the noise matching network L_3, C_3 is chosen around the optimum to tune out the source reactance $j\Delta$. This circuit shows proper impedance matching and lower power requirements, though it has the disadvantage of a complicated tuning procedure (figure 5.2).

Figure 5.3, indicates a circuit wherein the deringing, after the cessation of the pulse, is reduced using a pulse quench circuit with the switch S_Q . The configuration during reception is indicated in figure 5.3. The sources matched to $\lambda/4$ cable by the split capacitance pair C_2, C_m (used for transmitter matching). The cable with the crossed diode pair D is chosen to protect the receiver from the high power rf pulses. The transformer of turns ratio $1:n$ is used to effect noise matching with the preamplifier.

The design values are given in Table 5.2. While the circuit parameters L_2, C_2, C_m and n the turns ratio of the transformer are realizable, and the pulsed power requirement $W_p < 500W$, the reactive mismatch in Z_L is 10 ohms, which is a significant value. This is constrained by the problem of

pulse quenching. The requirement here is that the 'on' resistance of the quench switch must be smaller than the capacitive impedance. Ideally C_m is kept large enough to obtain a compromise between pulse deringing and reactance mismatch.

This problem is alleviated in a similar circuit by Kisman and Armstrong [32], by use of PIN diodes as a part of the resonant circuit to effect quenching. However the rf power dissipation and shot noise considerations ($\bar{i}_n^2 \sim 100 \text{ pA}/\sqrt{\text{Hz}}$) make its scope limited in the context. Hoult [33], presents a scheme, with PIN diodes turned off during reception. This circuit involves the use of four quarter wavelength sections ($\lambda/4 \sim 5 \text{ m}$ at 15 MHz), which is undesirable at the frequency of interest.

To sum up, the choice of coupling circuits with series resonance circuits involves a trade off between power matching pulse deringing and receiver noise figure requirements. Where the existence of good switches are assumed the scheme in figure 5.3, is feasible, else the first scheme may be resorted to.

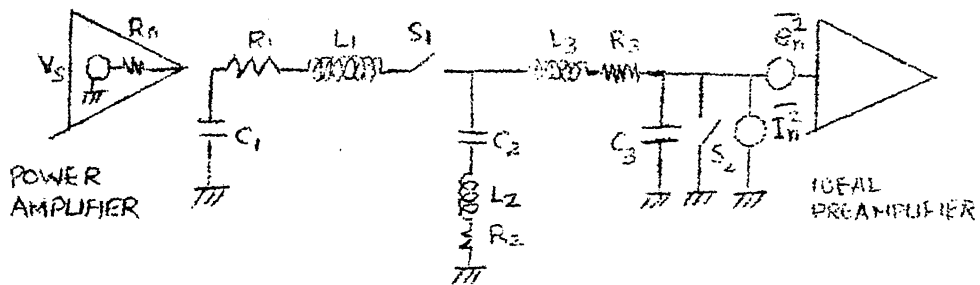
A wide band impedance transformer, reducing the source impedance of the amplifier ($R_o \sim 50 \text{ ohms}$) to a lower value, would introduce flexibility in the choice of the matching capacitance C_m . The matching need now be done for the receiver circuit only.

TABLE 5.1

SYSTEM SPECIFICATION

PARAMETER	VALUE	
T_2^* (for 0.05 G/cm)	2.27×10^{-4} sec	
T_2	50 μ Sec - 5mSec	
T_1	5mSec - 500mSec.	
T_e	~ 1 mSec	
τ_d	$\leq \frac{50 \times 10^{-6}}{100} \sim 0.5 \mu$ Sec.	
	SOLENOID	SADDLE SHAPED
R	$0.011 n^2 \Omega$	$0.176 n^2 \Omega$
L	$0.027 n^2 \mu H$	$0.099 n^2 \mu H$
Q_c max	200	32
C_d	~ 10 pf	≤ 10 pf
I_p	105.8/n A peak	70/n A peak
I_{avg}	$(\frac{1}{\sqrt{2}}) 106 \text{mA/n.}$ avg	$(\frac{1}{\sqrt{2}}) 70/n$. avg.
B_1	$2.22 \times 10^{-5} n$ tesla	$3.67 \times 10^{-5} n$ Tesla

(B_1 is calculated for $\phi = 90^\circ$, $T_p = 5$ sec).



CIRCUIT A : TRANSMITTER ON, S_1 ON, S_2 ON

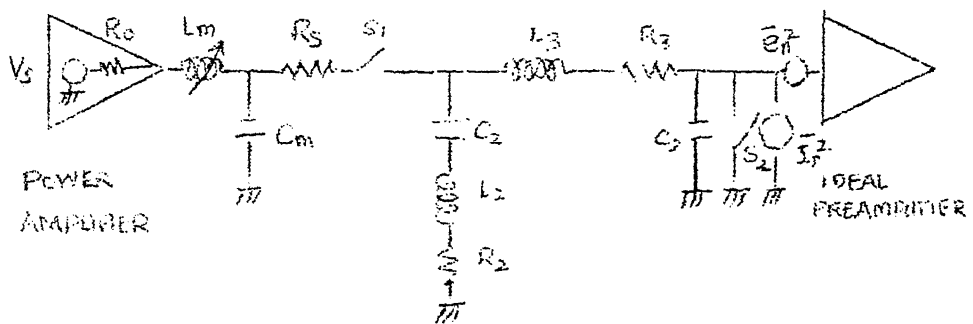
TRANSMITTER OFF, S_1 OFF, S_2 OFF

$$(L_1 C_1)^{-1} = (L_2 C_2)^{-1} = (L_3 C_3)^{-1} = \omega_0^2$$

L_2 IS THE SAMPLE COIL

FIGURE 5.1 : A SERIES RESONANCE COUPLING

CIRCUIT (CLARK AND MCNEILL [30])



$$\text{CIRCUIT B : } \omega L_2 - \frac{1}{\omega} \left(\frac{1}{C_m} + \frac{1}{C_2} \right) = 0$$

$$\omega L_m - \frac{1}{\omega C_m} = 0$$

R_s : 'Q' SPOILING RESISTANCE

FIGURE 5.2 : RESONANT CIRCUIT WITH POWER MATCHING

TABLE 5.2

CIRCUIT VALUE FOR A, B, and C.

Circuit Elements	A	B	C
R_2, L_2, C_2	0.4 μ H 112.5pf -1 Ω	0.4 μ H, 120pf -1 Ω $\Delta=5$	0.4 μ H 120pf -1 Ω
R_1, L_1, C_1, R_s	-, 0.3 μ H, 379pf 21 Ω	-	-
L_m, R_s, C_m	-	1.1 μ H, 10 Ω 105pf	0, 0, 1kpf
R_3, L_3, C_3	1 Ω , 1.7-2 μ H, 60-70pf	1 Ω , 1.7-2 μ H, 40-60pf	$n_{opt} = 22.5$
Z_L	38.5-j27.99 Ω	50 Ω	50 -j10.0 Ω
N_F	~6dB	~6dB	~6dB
W_p	~3.1kW	~1.5kW	~60-250W
W_{avg}	~3.1W	~1.5W	-
Q_T	6	≤ 10	Q_c
Q_R	≥ 50	≥ 50	~50

$$R_0 = 50 \Omega, \quad \omega = 2\pi \times 15 \times 10^6 \text{ rad/sec}$$

$$\tau_d = 0.5 \mu\text{Sec}, \quad n = 6$$

TABLE 5.2 (continued)

EQUATIONS FOR THE CIRCUITS A, B and C.

$$A : R_0 \leq \omega L_2 Q_T \leq 10 R_0$$

$$\omega \tau = 2 Q_T$$

$$L_1 = \left(\frac{L_2 R_0}{Q_T \omega} \right)^{\frac{1}{2}}, (R_1 + R_2) = \frac{\omega(L_1 + L_2)}{Q}$$

$$B_1 \geq 2/3 (B_1)_{\max}, L_3/C_3 = (R_2 + R_3) \bar{e}_n^> / \bar{I}_n^>$$

$$B : Z_L = \frac{\Delta}{\omega c_m (R_s + R_2)} - \frac{j}{\omega c_m}$$

$$c_m = \frac{\Delta}{\omega R_0 (R_s + R_2)}$$

$$\Delta \triangleq \omega L_2 - 1/\omega c_2$$

(c_m, c_2, L_2) , (c_m, L_3) and (c_2, L_2, c_3, L_3) are independently tuned at ω .

$$C : Z_L = \frac{\Delta}{\omega c_m R_2} - \frac{j}{\omega c_m}$$

$$c_m = \frac{\Delta}{\omega R_0 R_2}$$

$$\frac{1}{\omega c_m} \ll R_0$$

$$\Delta = \omega L_2 - \frac{1}{\omega c_2}$$

(c_m, c_2, L_2) are tuned.

CHAPTER 6

SUMMARY

6.1 DISCUSSION

The present work discusses the NMR imaging method from the point of view of system design. The observations ensuing from a mathematical model of the imaging system, and the system design considerations are discussed.

The model based on Bloch equations and rotating frame arguments show that,

1. The latter is a fairly useful tool in modelling different modalities in NMR imaging.

2. The response (namely the magnetic moment $m_{xy}(t)$) is linearly related to the system identification function $\rho(\vec{r}) L(\vec{r})$, while the aperture function is non-linearly related to the rf excitations.

3. The nonlinearity is found in the Bloch equations in the co-efficient $B_1(t)$. The solution for a rectangular excitation is possible in closed form, while for other pulses, it is obtained numerically.

4. The choice of pulses for signal design (in selective excitations) can be made by approximating the system by the linear term $M_{xy}^{(1)}(t)$ (section 3-4). The contribution of the linear term to the overall response is significant and is 30% for rectangular pulse excitations (90° flip).

5. Under white gaussian assumption (on the quadrature noise components), the estimate of the spin density function, for broad band excitations is

$$(w) = \varphi(w) + N(w) \text{ where } N(w) \text{ is a white gaussian process.}$$

The signal to noise ratio for a Zeugmatographic experiment is related to E_s/N_o (the signal energy-to-noise spectral density), as in finite time signals. The ratio is given by

$$E_s/N_o = \frac{w_o^2 B_1^2 V_s^2 \pi T_2^*}{N_o} \frac{B_1^2}{R_T},$$

for the case of a strong linear gradient and nominal contrast. This is similar to the SNR for a single pulse NMR experiment.

The system design considerations indicates that,

1. The hierarchy is in three levels, namely the application, object specification and system parameter specification respectively. This schematic is useful in design as well as in evaluating existing systems for a given task.

2. The distinction between the detection and display stages in imaging, enables the evaluation of the basic image quality (in terms of resolution and contrast) determined by the system hardware.

3. The resolution and contrast in the detection stage, are limited by noise. While in reality the two parameters are interrelated, a first order estimate is carried out by considering point pair resolution and noise (in terms of SNR) in isolation.

4. Two basic parameters associated with the detection stage are

- a. Signal to Noise Ratio
- b. The choice of operating frequency.

The maximum SNR obtainable in an imaging experiment has the following proportionalities

- a. Equilibrium magnetization ($\propto M_0$)
- b. Volume of the sample ($\propto V_s^2$)
- c. The signal decay time ($\propto T_2^*$)
- d. The frequency w_0 ($\propto w_0^{7/2}$)
- e. Signal averaging gain ($\propto G_{SA}$)

when the only non-ideality considered is the skin effect in the coil, which affects the figure of merit B_1^2/R_c .

At high frequencies where inductive losses in the sample are predominant, the frequency dependence becomes $w_0^{3/2}$. The SNR advantage in frequency, and the hardware complexity

(in terms of the magnet) define the optimum field range in imaging. For typical systems it is 3-4KG.

5. The received signal level is of the order of a microvolt, while the minimum transmitted power level required is $\sim \frac{1}{2} (2\phi/\gamma T_p)^2 \frac{R_v}{B_1^2}$ pulsed rms. This may be more than 1kW in typical systems. Considering the dissipation in other parts of the system, the total power required from the amplifier can be $< 10kW$.

For the case of imaging systems for multiphase bio-specimen,

1. Conventional pulsed, wideline NMR spectrometers may be modified for imaging.

2. A millimeter resolution is possible with a gradient of 0.5 G/cm, assuming a 200 Hz frequency resolution and signal averaging.

3. A feasible modality is the projection reconstruction technique, due to the simplicity of data acquisition.

4. The coupling circuits, with single coil probe, show stringent requirements in terms of impedance matching, power dissipation and post pulse deringing time. For large power requirement, adequate receiver isolation and quenching is called for.

5. The use of PIN diodes, for series transceiver gate and quench switches, is not desirable due to its large shot noise contribution ($\sim 100\text{pA}/\sqrt{\text{Hz}}$). Shunt switches are cumbersome for lower frequencies ($\sim 15\text{MHz}$), due to a number of $\lambda/4$ sections required. As such, where space is not a premium, crossed coils offer advantage in terms of convenient transceiver implementation.

6.2 SUGGESTIONS FOR FUTURE WORK

1. Evolution of the imaging equation covering situations such as the chemical shifts, which is especially relevant in study of in-vivo metabolism,

2. Identification of selective pulses using the linear assumption in Bloch equations, and numerical solutions.

3. Study of second order effects, such as gradient non-linearity, field fluctuations, and ~~rf~~ non-uniformity over the sample, in system identification.

4. Derivation of a contrast-resolution-SNR relationship for different imaging tasks, to determine realistic bounds on the performance of the system.

5. Designs of coils, for the magnetic fields ($H_0 < 6\text{KG}$) and $B_1(t)$, from homogeneity and SNR ($\propto B_1^2/R_c$), and linearity (in field gradient) considerations.

6. Design of a single coil probe, for imaging, catering to the impedance matching and deringing requirements.

7. A realistic analysis of the optimum field ranges, by simulation of different physiological samples.

REFERENCES

1. Lauterbur. P, 'Image Formation by Induced Local Interactions : examples employing NMR', Nature, Vol.242, No.5394, pp 190-191, March 1973.
2. Damadian. R, 'Tumor Detection by NMR', Science, Vol.171, No.3976, pp 1151-1153, March 1971.
3. Moss. A, 'Imaging Modalities', IEEE Trans., Medical Imaging, MI-1, No.4, pp 215-219, December 1982.
3. Macovski. A, 'Selective Rejection Imaging : Applications to Radiography and NMR', IEEE Trans., Medical Imaging, MI-1, No.1, pp 42-47, July 1982.
5. Ter-Pogossian. M.M., 'Engineering Research in Medical Imaging : A Synergistic Relationship', IEEE Trans., Medical Imaging, MI-1, No.4, pp 205-209, December 1982.
6. Cho Z.H. et.al., 'FT-NMR Tomographic Imaging', Proc. IEEE, Vol.70, No.10, pp 1152-1173, October 1982.
7. Kaufman et.al., 'Physical Basis of NMR Imaging', IEEE Trans., Nuclear Science, NS-29, No.3, p 1252, June 1982.
8. Scudder H.J , 'Introduction to Computer Aided Tomography', Proc. IEEE, Vol.66, No.6 , pp 628-637, June 1978.
9. Kaufman. L and Crooks L.E , 'Realistic Expectations for the Near Term Development of Clinical NMR Imaging', IEEE Trans., Medical Imaging, MI-2, No.2, pp 57-65, June 1983.

10. Andrew E.R , 'Nuclear Magnetic Resonance', Cambridge Monographs on Physics, Univ. Press 1956.
11. Ernst R.R. and Anderson W.A , 'Application of Fourier Transform Spectroscopy to Magnetic Resonance', Review of ~~Scientific Instruments~~, RSI-37, No.1, pp 93-102, January 1966.
12. Hoult D.I , 'Zeugmatography : Criticism of the Concept of Selective Pulses in the Presence of a Field Gradient', Journal of Magnetic Resonance , JMR-26, pp 165-167, 1977.
13. Locher P.R , 'Proton NMR Tomography', Philips Tech. Review, Vol. 41, No.3, pp 73-88, 1983-84.
14. Mansfield P. et.al., 'Fast Scan Proton Density Imaging by NMR', Journal of Physics, E. Sci - Instrum Vol.9, pp 271-278, April 1976.
15. Maudsley A.A , 'Multiple Line Scanning, Spin Density Imaging', Journal of Magnetic Resonance, JMR-41, No.1, pp 112-126, October 1980.
16. Kumar A. et.al., 'NMR Fourier Zeugmatography', Journal of Magnetic Resonance, JMR-18, No.1, pp 69-83, April 1975.
17. Hoult. D.I , 'The Solution of the Bloch Equation in the Presence of a Varying B_1 Field - An Approach of Selective Pulse Analysis', Journal of Magnetic Resonance, JMR-35, No.1, pp 69-86, July 1979.

18. Mansfield et.al., 'Selective Pulses in NMR Imaging A Reply to Criticism', Journal of Magnetic Resonance, JMR-33, No.2, pp 261-274, February 1979.
19. Caprihan. A, 'Effect of Amplitude Modulation on Selective Excitations in NMR Imaging', IEEE Trans, Medical Imaging, MI-2, No.4, pp 169-175, December 1983.
20. Hinshaw W.S. and Lent A.H., 'Bloch Equation and the Imaging Equation', IEEE Proc., Vol-71, No.3, pp 338-350, March 1983.
21. Silver et.al., 'Selective Pulse Creation by Inverse Solution of the Bloch - Riccati - Equation', Proc. 2nd Meeting, Society of Magnetic Resonance in Medicine, 1983.
22. Hoult D.I. and Richards R.E., 'The SNR of an NMR Experiment', Journal of Magnetic Resonance, JMR-24, No.1, pp 71-85, October 1976.
23. Hoult D.I. et.al., 'Electromagnet For Nuclear Magnetic Resonance Imaging', Review of Scientific Instruments, RSI-52, No.9, pp 1342-1351, September 1981.
24. Wagner R.F. and Brown D.G., 'Overview of a Unified SNR Analysis of Medical Imaging Systems'. IEEE Trans., Medical Imaging, MI-1, No.1, pp 210-214, December 1982.

25. House W.V., 'NMR Microscopy', IEEE Trans., Nuclear Science, NS-31, No.1, pp 570-576, February 1984.
26. Hoult D.I. and Lauterbur P.C., 'The Sensitivity of the Zeugmatographic Experiment Involving Human Samples', Journal of Magnetic Resonance, JMR-34, No.2, pp 425-433, May 1979.
27. Henney K. ed., 'Radio Engineering Handbook', McGraw Hill, 5th edition, 1959.
28. Ginzberg et.al., 'Optimum Geometry of Saddle Shaped Coils for Generating Uniform Magnetic Fields', Review of Scientific Instruments, RSI-41, No.1, pp 122-123, January 1970.
29. Bernardo Jr. M.L. et.al., 'Radiofrequency Coil Designs for Nuclear Magnetic Resonance Zeugmatographic Imaging', Proc. International Workshop on Physics and Engg. in Medical Imaging, March 1982.
30. Clark G.W. and McNeill J.A., 'Single Coil Series Resonant Circuit for Pulsed Nuclear Resonance', Review of Scientific Instruments, RSI-44, No.7, pp 844-857, July 1973.
31. Netzer Y., 'The Design of Low Noise Amplifiers', Proc. IEEE, Vol. 69, No.6, pp 728-741, June 1981.

32. Kisman K.E. and Armstrong R.L., 'Coupling Scheme and Probe Damper for Pulsed Nuclear Magnetic Resonance Single Coil Probe', Review of Scientific Instruments, RSI-45, No.9, pp 1159-1162, September 1974.
33. Hoult D.I. and Richards R.E., 'An Ultra High Frequency Receiver Scheme', Journal of Magnetic Resonance, JMR-22, No.1, pp 561-573, April 1976.
34. Brunner P. and Ernst R.R., 'Sensitivity and Performance Time in NMR Imaging', Journal of Magnetic Resonance, JMR-33, No.1, pp 83-106, January 1979.

APPENDIX A

ROTATING FRAME ARGUMENT (Rectangular pulse excitation)

Some details of the equations (2.7 - 3.9), of this thesis are provided here. The coordinates are labelled X', Y' and Z' . The two interacting magnetic fields in the rotating frame are :

1. ΔH , the residual field in the rotating frame
($=G_x x$, for a gradient along the X-axis).

2. $B_1(t)$, the rf modulating waveform ($=B_1$, a constant for $0 \leq t \leq T_p$ for a rectangular pulse).

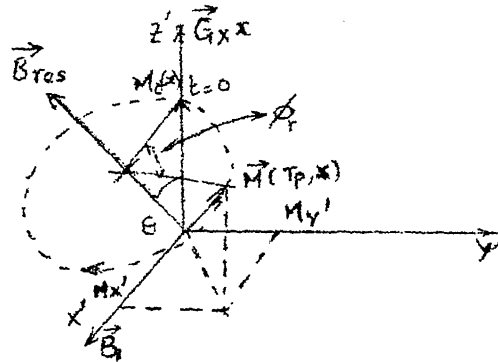


Figure A.1 Rotating Frame at Point x

For figure A.1,

$$|\vec{B}_{res}^>| = ((G_x x)^2 + B_1(t)^2)^{\frac{1}{2}}$$

$$\theta = \tan^{-1}(|\vec{B}_1^>(t)|/G_x(x)) \quad , \quad \text{the tilt angle}$$

$$\phi_r = \gamma |\vec{B}_{res}^>| T_p \quad , \quad \text{the flip angle.}$$

For a general initial condition, i.e., $\phi_1 = \phi|_{t=0} (\neq 0)$, the projections of the magnetization along the X' , Y' and Z' axes are,

$$M_{X'} = M_0(x) \left\{ \cos \xi \sin \theta - \sin \cos(\phi_1 + \phi_r) \cos \theta \right\}$$

$$M_{Y'} = M_0(x) \left\{ \sin \xi \sin(\phi_1 + \phi_r) \right\}$$

$$\text{and } M_{Z'} = M_0(x) \left\{ \sin \xi \cos(\phi_1 + \phi_r) \sin \theta + \cos \xi \cos \theta \right\}$$

where ξ is the semiconical angle (or the angle between the vectors $\vec{B}_{\text{res}}^>$ and $\vec{M}^>(r,t)$, and ϕ_r is the flip angle).

The projection or the aperture function $F(x)$, expressed in terms of $M_{X'}$ and $M_{Y'}$, is

$$\begin{aligned} \bar{F}(x) &= \frac{1}{M_0(x)} (M_{X'} - jM_{Y'}) \\ &= \sin \theta \cos \theta (1 - \cos \phi) - j \sin \theta \sin \phi \end{aligned}$$

for the condition $\phi_1 = 0$ and $\xi = \theta$.

Given $B_1 \gg G_x x$ (the broad band excitation), and $\phi_r = \pi/2$

$$F_x' = 0$$

$$\text{and} \quad F_y' = M_0(x) \quad \text{at} \quad t=T_p \quad (\text{A.1})$$

while for $B_1 \approx G_x x$

$$F_x'(x) = \sin \theta \cos \theta (1 - \cos \phi)$$

$$= \frac{B_1 |G_x x|}{\sqrt{B_1^2 + (G_x x)^2}} (1 - \cos \gamma \sqrt{B_1^2 + (G_x x)^2} T_p)$$

$$\text{and} \quad F_y'(x) = \sin \theta \sin \phi$$

$$= B_1 \gamma T_p \operatorname{sinc} (\gamma \sqrt{B_1^2 + (G_x x)^2} T_p)$$

(A.2)

The Bloch equations and the geometrical arguments may be related by the fact that, the former reflect the dynamics in the X', Y' and Z' frame, while the latter treats the problem in a frame tilted with respect to the X', Y' and Z' axes.

The vector $\vec{B}_{\text{res}}^>$ is along one of the axes of this frame. The trajectory of the magnetization can be treated as a free precession about the direction $\vec{B}_{\text{res}}^>$. Further the path may be referred to the rotating frame X', Y' , and Z' , through a

transformation of coordinates. Thus the solution of the Bloch equations is equivalent to a that of a solid geometry problem.

For example, for $\Delta H \ll B_{1\max}$, $M_y = -j M_0(x) \sin \phi$, as may be inferred from the geometric arguments. The same result is obtained by solving the Bloch equations (for $\Delta H=0$). The perturbation term $M^{(n)}$ (in equation 3.11), takes the form

$$M^{(n)} = -j \left(\frac{\phi^n}{n!} \right) (-1)^{\frac{n-1}{2}} M_0(x) \text{ for } n, \text{ odd and } n \geq 1.$$

This is the Taylor expansion for M_y . When $\Delta H \neq 0$, the perturbation series $M^{(n)}$ would converge to equation (A.2).

APPENDIX B

IMAGING EQUATIONS FOR SOME MODALITIES

1. RECONSTRUCTIVE TECHNIQUES

a. 3-D plane integral projections

$$m(t) = \int_{V_s} \rho(\vec{r}) e^{j\gamma(\vec{G}^>(\theta_n, \phi_m) \cdot \vec{r})t} dV \quad (B.1)$$

b. 2-D line integral projections

$$m(t) = K \Delta Z \int_{A_s} \rho(\vec{r}) e^{j\gamma(\vec{G}^>(\theta_n) \cdot \vec{r})t} dA \quad (B.2)$$

(the actual reconstruction is visualized in polar coordinates).

2. NON-RECONSTRUCTIVE TECHNIQUES

a. Sensitive point scanning

$$m(t) = \int \rho(\vec{r}) e^{j\gamma(A(x)x+B(y)+c(z)z) \cos wt} dV \quad (B.3)$$

(The frequency modulation may be noted)

b. Line scanning

$$m(t) = \iiint_{x_s y_s z_s} \rho(x, y, z) F_{xy}(z, z_0) F_{xy}(y, y_0) e^{j\gamma G_x x t} dx dy dz \quad (B.4)$$

(Here the readout gradient is in the x-direction)

3-D KWE Fourier Zeugmatography :

$$m(t) = \int_{V_s} \rho(x,y,z) e^{j\gamma(G_x x t_x + G_y y t_y + G_z z t_z)} dx dy dz \quad (B.5)$$

where t_x, t_y, t_z are 0 to t_a .

3. RECOVERY SEQUENCES

a. Saturation recovery :

$$m(t) = KA \int \rho(x) (1 - e^{-T_R/T_1(x)}) e^{j\gamma G_x x t} e^{-j\pi/2} dx$$

where ,

$$i) \quad T_R \sim \langle T_1(x) \rangle$$

$$ii) \quad F_{xy} = -j$$

and iii) Spin lattice relaxation has a exponential behaviour at point. x . (B.6)

b. Inversion Recovery :

At ~~time~~ $t = T_I$ after the 90° pulse, a broadband 180° pulse is applied,

$$M_z = -M_0(x) [1 - e^{-T_I/T_1(x)}]$$

and at $t = T$,

$$M_z(t, x)_{t=T} = M_z^0(T_I, x) e^{-T/T_1(x)} + M_0(x) (1 - e^{-T/T_1(x)})$$

$$\text{or } M_z(T, x) = M_0(x) [e^{-T/T_1(x)} (-2 + e^{-T_2/T_1(x)}) + 1] \quad (\text{B.7})$$

ERRATA

1. 'Plank' appearing in several places in this work should read 'Planck'.
2. 'Larmour' appearing in several places in this work, should read 'Larmor'.
3. 'Aquisition' appearing in several places in this work should read 'Acquisition'.
4. p.77, line 12: ' T_o ' should read ' T_c ' .
5. p.79, line 20)
 }
 }
and p.112, line 21) ' $w_o^{\frac{3}{2}}$ ' should read ' w_o^2 ' .
6. p.94, second row : under '~~C~~linical Imaging System',
 ' $f_o = 15 \text{ MHz}$ ' should read ' $f_o = 6 \text{ MHz}$ '.
7. p.110, line 22 : ' 30% ' should read ' 76% '.